

Data-Driven Stochastic Closure Modeling via Conditional Diffusion Model and Neural Operator

Xinghao Dong^a, Chuanqi Chen^a, Jin-Long Wu^{a,*}

^a*Department of Mechanical Engineering, University of Wisconsin–Madison, Madison, WI 53706*

Abstract

Closure models are widely used in simulating complex multiscale dynamical systems such as turbulence and the earth system, for which direct numerical simulation that resolves all scales is often too expensive. For those systems without a clear scale separation, deterministic and local closure models often lack enough generalization capability, which limits their performance in many real-world applications. In this work, we propose a data-driven modeling framework for constructing stochastic and non-local closure models via conditional diffusion model and neural operator. Specifically, the Fourier neural operator is incorporated into a score-based diffusion model, which serves as a data-driven stochastic closure model for complex dynamical systems governed by partial differential equations (PDEs). We also demonstrate how accelerated sampling methods can improve the efficiency of the data-driven stochastic closure model. The results show that the proposed methodology provides a systematic approach via generative machine learning techniques to construct data-driven stochastic closure models for multiscale dynamical systems with continuous spatiotemporal fields.

Keywords: Closure Model, Diffusion Model, Neural Operator, Stochastic Model, Non-local Model

1. Introduction

Complex dynamical systems are ubiquitous in a wide range of scientific and engineering applications, e.g., climate change prediction, renewable energy harvesting, and the discovery of materials for clean fuels and energy storage. These complex systems often feature a wide range of temporal and spatial scales, for which accurately resolving and coupling all of them is still infeasible for many real-world applications [1]. In practice, classical closure modeling approaches empirically avoid resolving some of the scales for affordable numerical simulations by introducing a closure model that accounts for the unresolved scales based on the resolved ones, such as Reynolds Averaged Navier-Stokes (RANS) [2, 3] and large eddy simulation (LES) closure models [4, 5]. However, a fundamental challenge in modeling the impacts of those small scales on large scales still exists when the complex system lacks a clear separation between resolved scales and unresolved ones. This challenge reveals the

*Corresponding author

Email address: jinlong.wu@wisc.edu (Jin-Long Wu)

limitations of classical closure models that often assume a deterministic model form and motivates the studies of stochastic models [6–15].

More recently, machine learning techniques have been explored to improve or even completely replace the classical closure models [12, 16–27], which demonstrates that the machine learning techniques can potentially leverage the rapid growth of data and lead to more sophisticated closure models than the classical approaches that mainly rely on domain knowledge and empirical calibration process based on a limited amount of data. However, most existing works still assume a deterministic model form, which may not well characterize the desired closure models if the resolved and unresolved scales do not have a clear scale separation [11].

On the other hand, generative models have distinguished themselves as powerful tools in machine learning tasks such as generating texts, images, and videos. Designed to approximate the underlying distribution of the training dataset and to sample from it efficiently, the generative models can also be used in the stochastic modeling of complex dynamical systems [28–32]. One standout subclass within generative models is diffusion models [33–37], which have demonstrated exceptional promise beyond traditional applications such as image and speech synthesis. The general concept of diffusion models is to gradually add noise to the target distribution via a diffusion process, which has a corresponding reverse Markov process that transforms the random noise back into a sample in the target distribution. The foundations of diffusion models can be traced to score matching [38] and its connection to denoising autoencoders [39], which laid the groundwork for various types of diffusion models. Key developments in diffusion models include denoising diffusion probabilistic models (DDPM) [33], which formalized the training and sampling processes, and denoising diffusion implicit models (DDIM) [40], which introduced faster deterministic sampling. In addition, score-based generative models were proposed by [36], and their unification with diffusion models through score-based SDEs [37, 41] has further advanced the field.

Compared to other generative models like Variational Autoencoders (VAEs) [42] and Generative Adversarial Networks (GANs) [43], diffusion models are not constrained by the need for specific model architectures to maintain a tractable normalizing constant, nor do they rely on the often unstable adversarial training methods. The structural flexibility of diffusion models allows for the incorporation of input conditions that can guide the generation process [44–46]. All these features of diffusion models highlight their potential for advancing the modeling of complex dynamical systems. The conditional score-based diffusion models for imputation (CSDI) [47] present an innovative method for time series imputation by leveraging score-based diffusion models. For prediction tasks, TimeGrad [48] leverages diffusion models and serves as an autoregressive model for time series forecasting. Additionally, DiffSTG [49] generalizes DDPMs to spatiotemporal graphs. Diffusion models have also been explored in applications of fluid dynamics, with the common goals of either directly generating spatiotemporal fields [50–52] or reconstructing high-fidelity spatiotemporal fields from the low-fidelity ones [53, 54]. Additionally, the integration of physics constraints and domain knowledge has been investigated in [55–57].

However, the use of diffusion models for closure modeling is still prevented by a common drawback of standard diffusion models, i.e., the slow sampling speed, which is mainly because diffusion models often require hundreds or even thousands of inference steps for the

generation of each sample. For a closure model, it needs to be evaluated at every numerical time step during the simulation, and thus standard diffusion models are too costly to serve as closure models. To address this drawback of diffusion models, some recent developments in acceleration techniques, such as distillation [58–60] and adaptive numerical schemes [61, 62], can be promising. One of the major goals of this work is to demonstrate the capability of diffusion models as stochastic closure models, utilizing these recent techniques to accelerate the sampling of diffusion models.

Furthermore, many interesting application areas of closure modeling involve continuous spatiotemporal fields, such as modeling turbulence in fluid dynamics. For these applications, standard diffusion models designed for images with finite resolutions (i.e., in a discretized vector space) can be insufficient. The recent development of continuous extensions of traditional neural networks (NN), known as neural operators [63–65], seeks to provide a continuous framework to capture the intrinsic multiscale nature of complex dynamical system states and associated data sources. Unlike traditional methods that are confined to a fixed mesh resolution, the adaptability of neural operators to different resolutions in training and testing enables them to handle data with different temporal and spatial resolutions efficiently. An example of neural operator is deep operator network (DeepONet) [63], which provides an architecture that consists of multiple deep neural networks – branch nets for encoding input functions and trunk nets for the output. On the other hand, the Fourier neural operator (FNO) [64] leverages Fourier transforms to construct a framework of approximating nonlinear operators. The merits of operator learning have been demonstrated in various applications involving partial differential equations such as solid mechanics, fluid dynamics, weather forecasting, and other fields where continuous spatiotemporal fields are of interest and capturing long-range interactions is essential [26, 66–69].

In this paper, we introduce a novel stochastic closure modeling framework for complex dynamical systems governed by PDEs. This modeling framework builds on the strengths of conditional diffusion models and operator learning techniques. More specifically, a score function constructed by the Fourier neural operator is trained to approximate the unknown score function that corresponds to a conditional probability distribution of the closure term. The score-based conditional diffusion model then serves as the data-driven stochastic closure and is deployed in the numerical simulations of the classical physics-based solver as an additional correction term. The key highlights of this work are summarized below:

- We develop a data-driven stochastic closure modeling framework for complex dynamical systems governed by PDEs, via training a score-based generative model that captures the conditional probability distribution of the unknown closure terms with respect to the known information, e.g., numerically resolved system states, sparse measurements of the true closure terms, and estimations from an existing physics-based closure model.
- We explore the Fourier neural operator to construct the score function in the generative model, which leads to two advantages: (i) the resolution invariance property that facilitates using data with various resolutions, and (ii) the non-local property that goes beyond the assumption of a local closure model.

- We proposed a rapid sampling strategy that accelerates the sampling speed of the data-driven stochastic closure model by up to a factor of $O(100)$, significantly enhancing the practicality of diffusion models being used in the context of stochastic closure modeling.

2. Methodology

The governing equation of a dynamical system in general form studied in this work can be written as:

$$\frac{\partial v}{\partial t} = M(v), \quad (1)$$

where v denotes the system state and M represents the dynamics derived from first principles, which can involve highly nonlinear mappings, differential operators, and integral operators. In practice, numerically resolving every detail of v can be infeasible, which motivates the focus on a reduced-order system:

$$\frac{\partial V}{\partial t} = \widetilde{M}(V), \quad (2)$$

where $V := \mathcal{K}(v)$ denotes a reduced-order representation of v with a map \mathcal{K} that extracts the information to be numerically resolved, and $\widetilde{M}(V)$ is derived based on domain knowledge to approximate the reduced-order dynamics $\mathcal{K} \circ M(v)$, so that a closed system of V is obtained for practical numerical simulations. To enhance the performance of the classical closure models \widetilde{M} , researchers have recently explored introducing a machine-learning-based correction term U , with the aim that $\widetilde{M}(V) + U$ can potentially better characterize the actual reduced-order dynamics.

In this work, we focus on a stochastic form of the correction term U enabled by the recent developments of diffusion models. More specifically, we aim to approximate the distribution $p(U)$ and to efficiently sample from it. It should be noted that U often depends on the current state V and potentially other information, such as the temporal history of V or the spatially non-local information. Therefore, we denote all the dependent information of a well-characterized correction term U as y and focus on a conditional diffusion model framework that targets the approximation and efficient sampling of $p(U | y)$.

The proposed stochastic closure modeling framework is illustrated in Fig. 1, with key components further introduced in Sections 2.1 to 2.3. The associated algorithms are described in Appendix C.

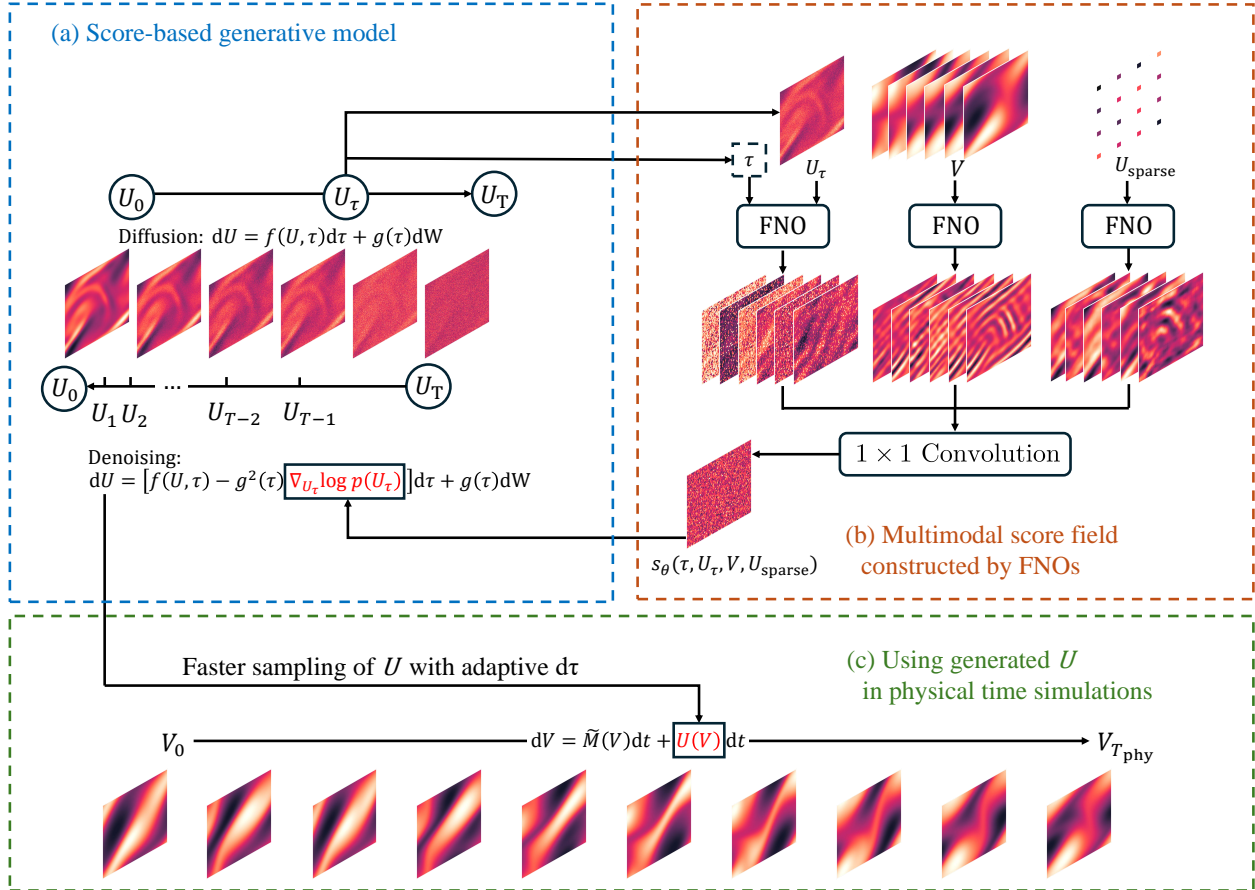


Figure 1: A schematic of the proposed framework for stochastic closure modeling via score-based generative model and Fourier neural operator. The score function with multimodal inputs is constructed by FNOs and deployed in a conditional diffusion model, with which samples can be generated to serve as a data-driven closure term for a complex dynamical system whose dynamics are only partially known or even completely unknown.

2.1. Score-Based Generative Model

Instead of directly approximating the probability distribution function, score-based models leverage available independent identically distributed (i.i.d.) data samples to learn the score function $\nabla_U \log p(U)$, defined as the gradient of the log probability density function [70, 71]. Unlike the probability density function, the score function does not require a tractable normalizing constant and can be trained with samples of U by score matching [39, 72]. Once the score function is trained, the sampling from $p(U)$ can be achieved via Langevin dynamics [73, 74], usually beginning with samples from an easy-to-sample distribution, e.g., a Gaussian distribution. In practice, U is often high-dimensional, and it is infeasible to have enough data to guarantee an accurate trained score function within the entire high-dimensional space.

To address the challenge of inaccurate score estimation in some regions of low-density or sparse data [36], one strategy involves progressively adding noise to the initial distribution and training the score-based model on these perturbed data points. In a continuous-time framework, the process of noise adding is achieved by a stochastic differential equation

(SDE) [37]:

$$dU = f(U, \tau)d\tau + g(\tau)dW. \quad (3)$$

Here, W denotes a Wiener process, and $\tau \in [0, T]$ represents the time in the SDE simulation, which is usually incorporated as an input into the score-based model as an indicator of noise levels. The choice of the detailed forms for f and g in this SDE is not unique. A common choice is known as the variance exploding (VE) SDE [37]:

$$dU = \sigma^\tau dW, \quad (4)$$

with σ as a constant scalar. This is equivalent to defining a Gaussian transition kernel in this form:

$$p(U_\tau | U_0) = \mathcal{N}(\mu(U, \tau), \Sigma(\tau)), \quad (5)$$

where

$$\mu(U, \tau) = U_0, \quad (6)$$

$$\Sigma(\tau) = \frac{1}{2 \log \sigma} (\sigma^{2\tau} - 1) I. \quad (7)$$

At $\tau = 0$, the distribution $p(U_0)$ corresponds to the true data distribution. With the transition kernel defined in Eq. (5), the final distribution after the diffusion process introduced in Eq. (4) can also be derived analytically:

$$p(U_T) = \int p(U_0) \cdot \mathcal{N}\left(U_0, \frac{1}{2 \log \sigma} (\sigma^{2T} - 1) I\right) dU_0 \approx \mathcal{N}\left(0, \frac{1}{2 \log \sigma} (\sigma^{2T} - 1) I\right). \quad (8)$$

When $\tau = T$ and σ are sufficiently large to ensure enough amount of noise is added, $p(U_T)$ approaches a zero-mean Gaussian distribution, which is easy to sample from. With samples from the distribution $p(U_T)$, the samples from the target distribution $p(U_0)$ can be obtained by solving the following reverse SDE [75]:

$$dU = [f(U, \tau) - g^2(\tau)\nabla_{U_\tau} \log p(U_\tau)] d\tau + g(\tau)dW, \quad (9)$$

from $\tau = T$ to $\tau = 0$, and the score function $\nabla_{U_\tau} \log p(U_\tau)$ can be approximated by a neural network, which can be trained via score matching. The standard score matching and the denoising score matching [39, 72] have the following equivalency:

$$\mathbb{E}_{U_\tau \sim p(U_\tau)} \|\nabla_{U_\tau} \log p(U_\tau) - s_\theta\|_2^2 = \mathbb{E}_{U_\tau \sim p(U_\tau|U_0)} \mathbb{E}_{U_0 \sim p(U_0)} \|\nabla_{U_\tau} \log p(U_\tau | U_0) - s_\theta\|_2^2 + C, \quad (10)$$

where the left-hand and right-hand sides correspond to the explicit and denoising score matching, respectively, with s_θ representing the model to be trained and C being a constant independent of θ . It is worth noting that the true score function required by the explicit score matching is often inaccessible, and thus denoising score matching provides a practical way of obtaining a neural network s_θ that approximates the true score function. With an adequately

expressive model and a sufficient enough dataset, the above equivalency ensures that a score-based model $s_\theta(\tau, U_\tau)$ trained with the following denoising score matching objective function

$$\theta^* = \arg \min_{\theta} \left\{ \mathbb{E}_{\tau \sim \mathcal{U}(0, T)} \mathbb{E}_{U_\tau \sim p(U_\tau | U_0)} \mathbb{E}_{U_0 \sim p(U_0)} \|\nabla_{U_\tau} \log p(U_\tau | U_0) - s_\theta(\tau, U_\tau)\|_2^2 \right\} \quad (11)$$

will effectively approximate the score function $\nabla_{U_\tau} \log p(U_\tau)$ for almost all U_τ and $\tau \in [0, T]$. Detailed proofs can be found in [Appendix A.1](#).

In this work, we focus on the use of score-based diffusion models for closure modeling, which aims to provide a correction term U to the right-hand side of Eq. (2), such that the numerical simulation would lead to resolved system state V that has a better agreement with the true one. In many applications, it is expected that the correction term U should depend on the resolved system state V and can benefit from the knowledge of some other information, such as the estimation of U from existing physics-based models or sparse measurements of true U from the real system. Therefore, a conditional diffusion model is needed to account for all the dependent information to better characterize the correction term U for the modeled system in Eq. (2). The conditional score-based model [47, 53, 54, 57] is designed to learn the score function of a conditional distribution $p(U | y)$, which is represented as $\nabla_U \log p(U | y)$. Here, y denotes the dependent information in general that are helpful for characterizing the closure model.

Challenges in transitioning to the conditional model involve expectations of the conditional transitional kernel $U_\tau \sim p(U_\tau | U_0, y)$ and a conditional initial distribution $U_0 \sim p(U_0 | y)$. The forward SDE in a diffusion process operates as a Markov chain, meaning the transition kernel is unaffected by any input conditions y , which implies that $p(U_\tau | U_0, y) = p(U_\tau | U_0)$. In the objective function, we choose to take the expectation of a more tractable joint distribution $p(U_0, y)$, instead of the conditional distribution $p(U_0 | y)$. Detailed derivations are provided in [Appendix A.2](#), and the objective function in the conditional model setting is presented below:

$$\theta^* = \arg \min_{\theta} \left\{ \mathbb{E}_{\tau \sim \mathcal{U}(0, T)} \mathbb{E}_{U_\tau \sim p(U_\tau | U_0)} \mathbb{E}_{U_0, y \sim p(U_0, y)} \|\nabla_{U_\tau} \log p(U_\tau | U_0) - s_\theta(\tau, U_\tau, y)\|_2^2 \right\}. \quad (12)$$

Once the score function $s_\theta(\tau, U_\tau, y)$ is trained based on the above objective function, the sampling process involves solving the backward SDE defined in Eq. (13) from $\tau = T$ to $\tau = 0$, with the score function being replaced by the conditional one $\nabla_{U_\tau} \log p(U_\tau | y)$. Associated with the VE SDE in Eq. (4), the backward SDE has the analytical form of

$$dU = -\sigma^{2\tau} \nabla_{U_\tau} \log p(U_\tau | y) d\tau + \sigma^\tau dW. \quad (13)$$

One common choice for solving Eq. (13) is the Euler-Maruyama numerical scheme, which can be expressed as

$$\begin{aligned} U_{\tau-\Delta\tau} &= U_\tau + \sigma^{2\tau} \nabla_{U_\tau} \log p(U_\tau | y) \Delta\tau + \sigma^\tau \sqrt{\Delta\tau} z \\ &\approx U_\tau + \sigma^{2\tau} s_\theta(\tau, U_\tau, y) \Delta\tau + \sigma^\tau \sqrt{\Delta\tau} z, \end{aligned} \quad (14)$$

with $z \sim \mathcal{N}(0, I)$, where the true score function is approximated by the trained neural network model s_θ , which depends on the noise level τ , the intermediate noisy state U_τ , and other conditional inputs y .

2.2. Neural Operator for the Construction of Score Function

In this work, we focus on the complex dynamical systems governed by PDEs, whose true system state v in Eq. (1) and the resolved system state V in Eq. (2) are both continuous spatiotemporal fields. Instead of using a standard diffusion model designed for images in finite vector spaces, a Fourier neural operator [64] is employed to construct the score function, which not only enables a generative diffusion model for continuous spatiotemporal fields but also facilitates the learning of a non-local closure model if needed. It is worth noting that non-locality in space and/or time is important for the modeling of many complex dynamical systems and the general concept of non-local models can be found in [15, 76–82].

The standard Fourier neural operator is represented by a sequence of N Fourier layers, with the detailed form of the n -th layer defined below:

$$Q_{n+1}(\mathbf{x}) = \sigma(LQ_n(\mathbf{x}) + (KQ_n)(\mathbf{x})), \quad n = 0, 1, \dots, N - 1, \quad (15)$$

where σ is the activation function and L is a linear transformation. K is defined as the Fourier integral operator, $(KQ_n)(\mathbf{x}) = \mathcal{F}^{-1}(R \cdot (\mathcal{F}Q_n))(\mathbf{x})$ with R being the complex-valued parameters in the neural network, and \mathcal{F} with \mathcal{F}^{-1} denoting the Fourier transform and inverse Fourier transform, respectively.

As shown in Fig. 1, FNOs are used to construct the score-based model $s_\theta(\tau, U_\tau, \mathbf{y})$, which takes noise level τ , corresponding perturbed target field U_τ , and a set of conditions \mathbf{y} as inputs. Our architecture involves a combination of multiple FNO pipelines, which are designed to handle different inputs to the score-based model.

The noise levels, indicated by the SDE time information τ , are incorporated via Gaussian random features as described in [83]. For a given SDE time scalar τ , it is processed by Gaussian Fourier projection in the form of

$$r(\tau) = [\sin(2\pi\gamma\tau); \cos(2\pi\gamma\tau)], \quad (16)$$

where $[\cdot; \cdot]$ denotes the concatenation of two vectors, and γ represents fixed, non-trainable Gaussian weights that are randomly sampled during initialization. The features $r(\tau)$ are then further processed by applying an activation function, followed by a linear layer and a dense layer, resulting in a rich embedding that can be incorporated into the FNO pipelines. This allows the model to learn the dependency between noise levels τ and corresponding diffused states U_τ .

FNO is suitable to construct resolution-invariant and non-local models that involve spatially continuous fields, and we construct an FNO-based multimodal score function with three types of inputs: (i) the associated intermediate diffusion states U_τ , (ii) the related resolved system states V , and (iii) other useful information to characterize the desired closure term U , such as the sparse measurements of true U or the estimation of closure term via physics-based models as additional conditional inputs in \mathbf{y} . In practice, the sparse information of true closure term U may not be directly measurable, but it can still be estimated based on sparse measurements of the original system state v . In terms of the associated intermediate diffusion states U_τ , the resolved system states V , and the estimation of closure term via physics-based models, they often share the same spatial resolution as the desired true closure term, and

thus standard FNOs can be employed to handle each of them. On the other hand, the sparse measurements of the true closure term likely have a different spatial resolution and thus require numerical upscaling methods before being fed into a standard FNO as input. Finally, all information obtained from the multiple parallel pipelines of FNO is concatenated and convolved to produce the final output of the score function estimation, which is then optimized through the denoising score matching shown in Eq. (12), and an illustration of using FNOs to construct the score function is presented in Fig. 1.

It is worth noting that the desired correction term $U(\mathbf{x}, t_n)$ can also depend on a time series of its historical snapshots

$$\{U(\mathbf{x}, t) \mid t \in [t_m, t_n) \text{ with } t_m, t_n \in [0, T_{\text{phy}}] \text{ and } t_m < t_n\}, \quad (17)$$

and a time series of historical data of resolved system states V :

$$\{V(\mathbf{x}, t) \mid t \in [t_m, t_n) \text{ with } t_m, t_n \in [0, T_{\text{phy}}] \text{ and } t_m < t_n\}, \quad (18)$$

where t and T_{phy} are defined as the physical time. To handle time series of spatial fields as conditional inputs, a 3-D FNO [64] that convolves both spatially and temporally can be utilized.

2.3. Fast Sampling Strategies

If $\tau = T$ and σ are sufficiently large, the prior distribution in Eq. (8) becomes an easy-to-sample Gaussian distribution. Therefore, the sampling process from the desired distribution by using a score-based diffusion model only requires numerically simulating the reverse SDE in Eq. (13). However, this simulation-based sampling process can be too costly when it serves as a stochastic closure model, which demands a new sample generated by the conditional diffusion model for each time step in the simulation of the model system in Eq. (2). For instance, the backward SDE using the Euler-Maruyama solver in Eq. (14) often requires thousands or even more time steps to ensure the quality of a generated sample.

In this section, we introduce a fast sampling strategy that speeds up the sampling process by a factor of $O(100)$. This substantial improvement is partly due to the adoption of adaptive time step size in Euler-Maruyama solvers, inspired by the findings of Karras et al. [62]. Instead of using uniform step sizes, we utilize a scheduling function to monotonically decrease the step sizes as the simulation progresses from $\tau = T$ to $\tau = 0$. The scheduling function is defined as:

$$\tau_{i < N} = \left(\tau_{\text{max}}^{\frac{1}{\rho}} + \frac{i}{N-1} \left(\tau_{\text{min}}^{\frac{1}{\rho}} - \tau_{\text{max}}^{\frac{1}{\rho}} \right) \right)^{\rho} \quad (19)$$

with $\rho = 7$, $\tau_{\text{max}} = T$, $\tau_{\text{min}} = 10^{-3}$, $\tau_N = 0$, and N is the number of desired steps. In the numerical scheme outlined in Eq. (14), although larger step sizes can introduce greater numerical errors, the quality of a generated sample at the end is not sensitive to those errors due to the high noise levels at earlier stages. The noise at earlier stages of the backward SDE effectively dominates the errors introduced by larger time steps, as changes in the system state are mainly dictated by the added noise through the forward SDE, rather

than the accuracy of the numerical solver for the backward SDE. As τ decreases and noise levels gradually diminish, the accuracy of the backward SDE solver becomes increasingly crucial, which demands smaller time steps. The adaptive time-stepping approach in Eq. (19) ensures that the solver’s performance balances efficiency and accuracy throughout the whole simulation of the backward SDE from $\tau = T$ to $\tau = 0$.

Another enhancement to speed up the sampling process is using a smaller T enabled by the incorporation of conditional inputs in the diffusion model. Starting from a prior distribution that is closer to the ground truth data distribution (e.g., $T = 0.1$ instead of $T = 1$) helps to reduce the computational cost of solving the backward SDE. The improvement was made possible because the incorporated conditions can mitigate the need to explore the entire high-dimensional data space that usually requires highly perturbed distributions, i.e., larger T for the forward SDE in a diffusion model. When the relationships between conditions and targets are deterministic, the conditional distribution becomes degenerate, allowing for precise sample generation from any starting prior distribution. By focusing on a smaller regime of the data space, conditional models improve the efficiency and accuracy of the generation process, eliminating the need to cover broader data spaces as unconditional models have to do.

3. Numerical Results

In our numerical examples, we consider the following stochastic 2-D Navier-Stokes equation:

$$\begin{aligned} \frac{\partial \omega(\mathbf{x}, t)}{\partial t} &= -u(\mathbf{x}, t) \cdot \nabla \omega(\mathbf{x}, t) + f(\mathbf{x}) + \nu \nabla^2 \omega(\mathbf{x}, t) + \beta \xi, & (t, \mathbf{x}) \in (0, T_{\text{phy}}] \times (0, 1)^2 \\ \nabla \cdot u(\mathbf{x}, t) &= 0, & (t, \mathbf{x}) \in (0, T_{\text{phy}}] \times (0, 1)^2 \\ \omega(\mathbf{x}, 0) &= \omega_0(\mathbf{x}), & \mathbf{x} \in (0, 1)^2 \end{aligned} \quad (20)$$

where u represents the divergence-free velocity field, $\omega = \nabla \times u$ denotes the vorticity of a fluid flow, ν denotes the viscosity coefficient and is set to 10^{-3} in this example. The 2D Navier-Stokes system is considered with periodic boundary conditions, with the initial vorticity $\omega(0, \mathbf{x}) = \omega_0(\mathbf{x})$ generated from a 2-D Gaussian random field $\omega_0 \sim \mathcal{N}(0, 7^{3/2}(-\Delta + 49I)^{-5/2})$, where Δ is the Laplace operator and I is the identity operator. f here represents a deterministic forcing of the form $f(\mathbf{x}) = 0.1(\sin(2\pi(x + y)) + \cos(2\pi(x + y)))$, which is a function of space coordinates $\mathbf{x} = (x, y)$. The stochastic forcing ξ is defined as $\xi = dW/dt$ with W being a Wiener process and rescaled by a coefficient $\beta = 5 \times 10^{-5}$.

We numerically solve Eq. (20) using a pseudo-spectral solver described in [Appendix B.1](#) and time is advanced by the Crank-Nicolson method described in [Appendix B.2](#) with a uniform resolution of 256×256 and a fixed time step $\Delta t = 10^{-3}$. System states and other needed properties are recorded every 10 time steps, i.e. a physical time unit of 10^{-2} s, for producing the training and test data. We simulate a total of 10 time series each with a physical temporal length of 40 seconds but only use the snapshots between 30s and 40s for training and testing. This is because the initial period of the simulation, from 0s to 30s, is used to allow the system to warm up and reach a more stable state, avoiding the influence of initial transient results. For the training data, we use the first 8 time series, while reserving

2 time series for testing. The high-fidelity data is first evenly sub-sampled to 64×64 . For testing, we evaluate our model’s performance and confirm the resolution invariance using three different data resolutions: 64×64 , 128×128 and 256×256 .

For the numerical examples in this work, we focus on the setting that the right-hand side of Eq. (20) is only partially known, with stochastic viscous diffusion term $G(x, t) = \nu \nabla^2 \omega(x, t) + 2\beta\xi$ assumed to be unknown, for which a closure model is needed. More specifically, a conditional diffusion model will be trained to approximate the contribution of those two unknown terms, and we mainly focus on three objectives:

- Our primary objective is to investigate the performance of the continuous stochastic modeling framework. The framework aims to provide samples of G by training a score-based diffusion model, which utilizes architecture of FNOs to construct the score function and is conditioned on the vorticity $\omega(x, t)$ and sparse observations of $G^\dagger(x, t)$, where \dagger denotes the quantities of the true system. Results of the sampled G are in Section 3.1.
- We further investigate and confirm that the continuous stochastic modeling framework is resolution-invariant, by training a model based on data with one resolution and testing the model based on data with a few choices of resolutions. The results are summarized in Section 3.2.
- We also incorporate the fast sampling technique discussed in Section 2.3 and employ the trained diffusion model as an efficient data-driven closure for the stochastic viscous diffusion term in Eq. (20). The accuracy of the simulated vorticity fields and the speedup of the simulations compared to the standard sampling techniques are summarized in Section 3.3.

To quantitatively evaluate the performance of the generated results, we first use the normalized mean squared error (MSE) defined as

$$D_{\text{MSE}}(G^\dagger, G) = \frac{\|G^\dagger - G\|_2^2}{N}, \quad (21)$$

where $\|G^\dagger - G\|_2^2$ represents the squared Euclidean norm (L_2 norm) of the difference between the ground truth G^\dagger and the generated field G . N denotes the total number of grid points. This metric provides a measure of the average squared error per grid point.

We also adopt the relative L_2 error which is defined as

$$D_{\text{RE}}(G^\dagger, G) = \frac{\|G^\dagger - G\|_2}{\|G^\dagger\|_2}. \quad (22)$$

This metric provides a measure of the relative error (RE) between the ground truth G^\dagger and the predicted G , normalized by the magnitude of the ground truth G^\dagger . For the simulation results of the vorticity ω , the MSE and RE are defined in similar ways as Eqs. (21) and (22).

To further confirm the resolution invariance property, we also study the energy spectrum between the true fields and the generated ones. The energy spectrum is defined as:

$$E(k, t) = \frac{1}{2} \left| \hat{G}(k, t) \right|^2, \quad (23)$$

where $\hat{G}(k, t) = \mathcal{F}(G(x, t))$ denotes the Fourier transform of the field $G(x, t)$ with k as the wavenumber. $|\cdot|$ evaluates the magnitude of a complex number.

3.1. Conditional Generation of the Stochastic Viscous Diffusion Term

Based on the proposed diffusion model architecture in Fig. 1, we first train a conditional diffusion model for the stochastic viscous diffusion term $G^\dagger(x, t)$ in Eq. (20). Figure 2 presents the test data results of the stochastic viscous diffusion terms of the true system and the generated ones, which are based on the trained conditional diffusion model that is only conditioned on the vorticity field ω at the current time. As shown in Fig. 2, the discrepancies between the ground truth $G^\dagger(x, t)$ and the generated samples $G(x, t)$ remain significant when the diffusion model is conditioned solely on the current vorticity $\omega(x, t)$. The average D_{MSE} across all batches is 2.9423×10^{-3} with an average D_{RE} of 0.4316.

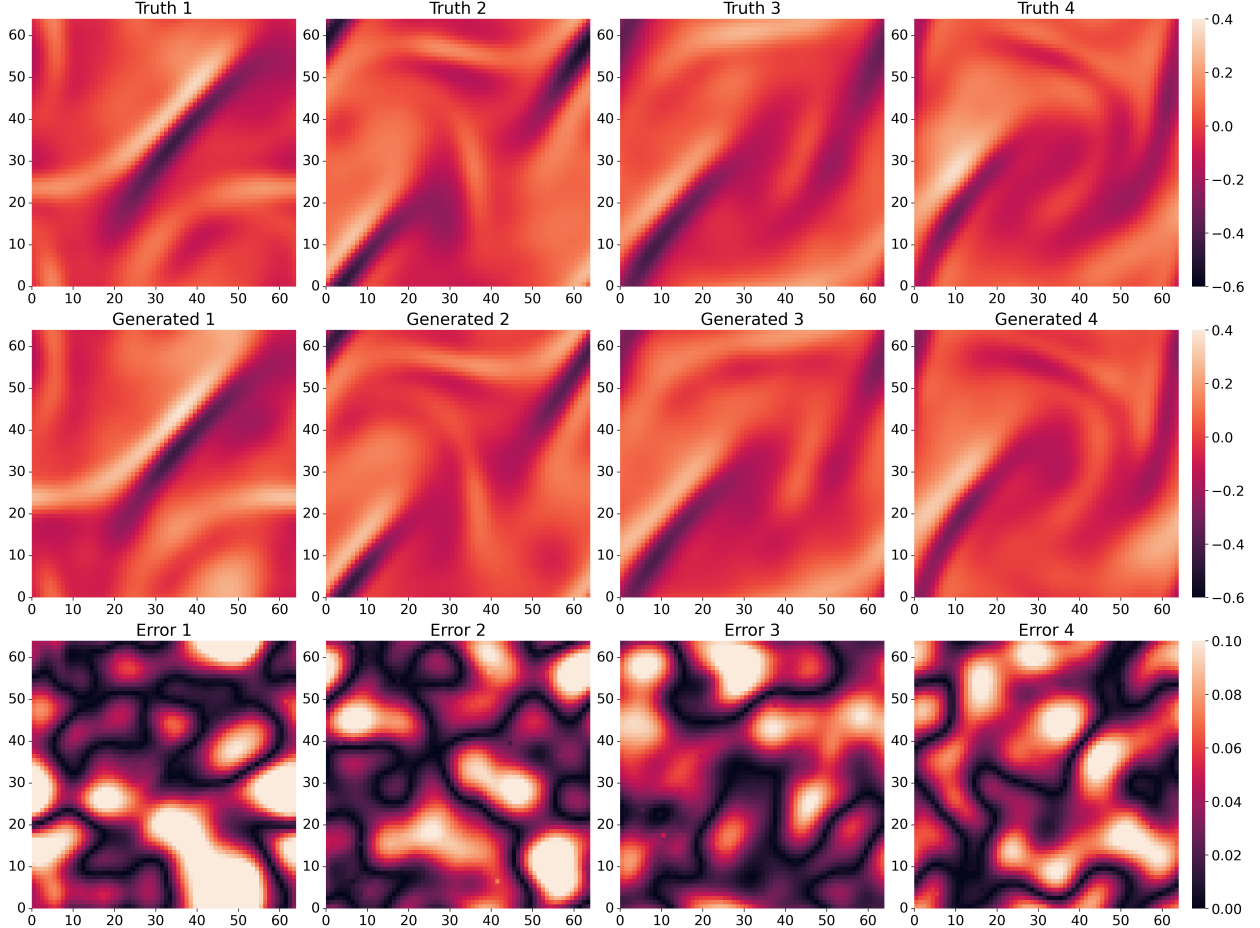


Figure 2: Generated $G(x, t)$ without sparse information and conditioned only on current vorticity ω . Training data resolution: 64×64 . Test data resolution: 64×64 . First row: random samples of the ground truth G^\dagger . Second row: corresponding generated samples G . Third row: absolute error fields between G^\dagger and G . The indices 1 to 4 correspond to different snapshots randomly sampled from the test dataset.

To enhance the model’s capability in capturing the information in the ground truth $G^\dagger(x, t)$, we further incorporate sparse observations of $G^\dagger(x, t)$ as an extra conditional input into the current model setup. Given sparse observation vectors $G^\dagger_{\text{sparse}}$ (with a resolution of 16×16 in this work), multiple methods are available for upscaling the sparse measurements to match the resolution of the model (64×64), including interpolation and convolution. However, as shown in Table 1, these methods alone are insufficient for accurately reconstructing the field based on the sparse measurements. The upscaling of sparse measurements is achieved through two commonly used techniques: (i) bicubic interpolation and (ii) 2-D convolution.

Table 1: Errors of upscaled sparse observation of the ground truth $G^\dagger_{\text{sparse}}$ from the resolution of 16×16 to the one of 64×64 via bicubic interpolation and 2-D convolution.

Methods \ Errors	Test Data		Test Errors	
	dx	dy	D_{MSE}	D_{RE}
Bicubic interpolation	1/64	1/64	5.6571e-03	0.6095
2-D convolution	1/64	1/64	3.8543e-03	0.5007

On the other hand, we demonstrate that incorporating upscaled sparse measurements as an additional input condition of the proposed conditional diffusion model effectively enhances the model’s performance to reconstruct the ground truth $G^\dagger(x, t)$. The improvements in the quality of the generated samples are confirmed by Fig. 3 and Fig. 4, both of which provide smaller absolute error fields compared to the ones in Fig. 2. As summarized in Table 2, the conditional diffusion model without the sparse information of G^\dagger struggles to provide a reliable generative model for the stochastic viscous diffusion term, resulting in a high relative error. However, when the model is conditioned on both vorticity $\omega(x, t)$ and upscaled sparse information of $G^\dagger_{\text{sparse}}(x, t)$, the accuracy of the generated samples significantly improves. The main reason is that conditioning on sparse information of G^\dagger avoids the need to accurately train the score function within the whole high-dimensional probability space and only focuses on those highly correlated regimes with respect to the incorporated sparse information of G^\dagger , and thus better performance can be expected with a limited amount of data.

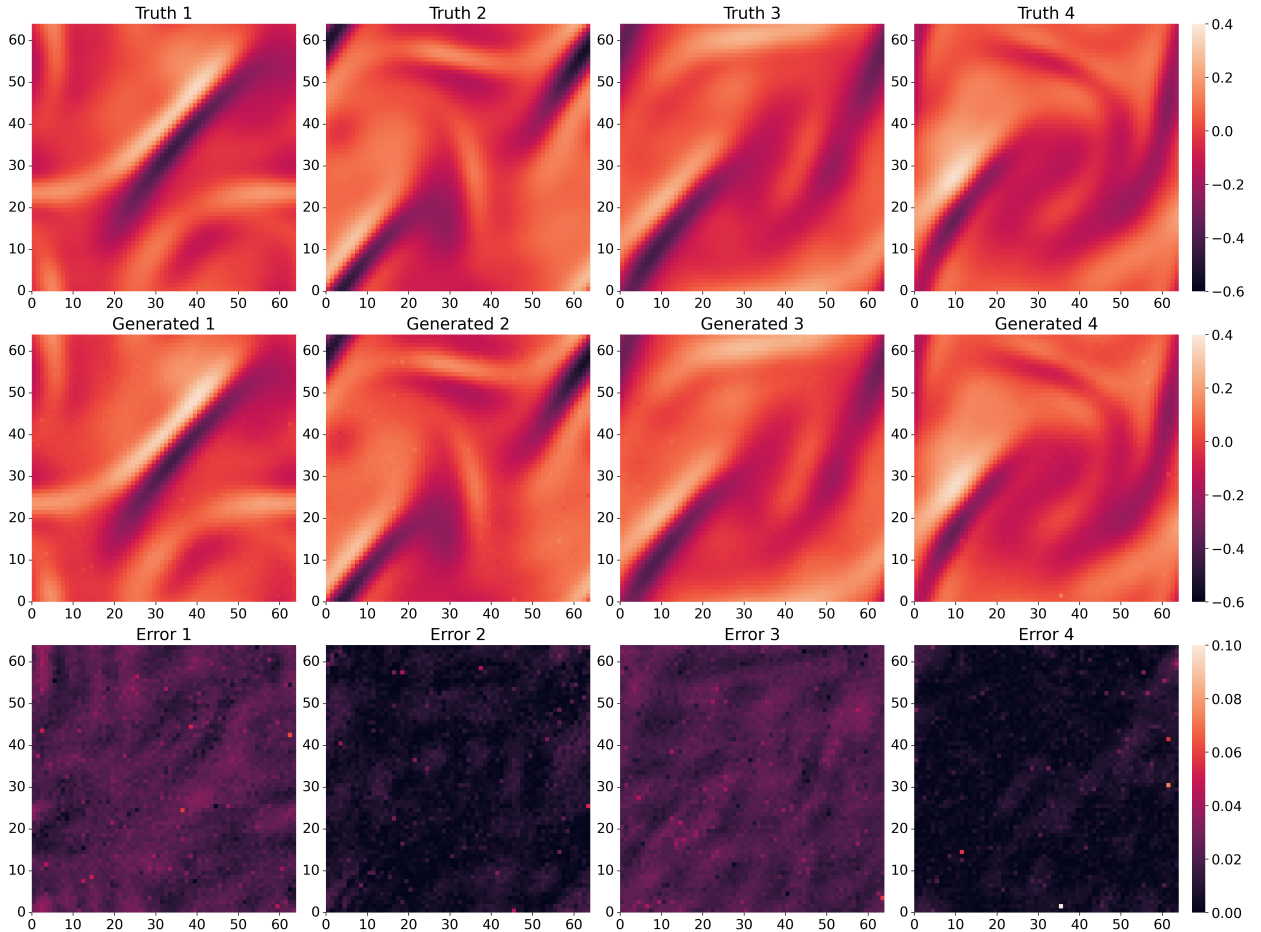


Figure 3: Generated $G(x, t)$ conditioned on current vorticity ω and sparse information of $G^\dagger_{\text{sparse}}$. Sparse information is upscaled using bicubic interpolation. Training data resolution: 64×64 . Test data resolution: 64×64 . First row: random samples of the ground truth G^\dagger . Second row: corresponding generated samples G . Third row: absolute error fields between the ground truth G^\dagger and generated G .

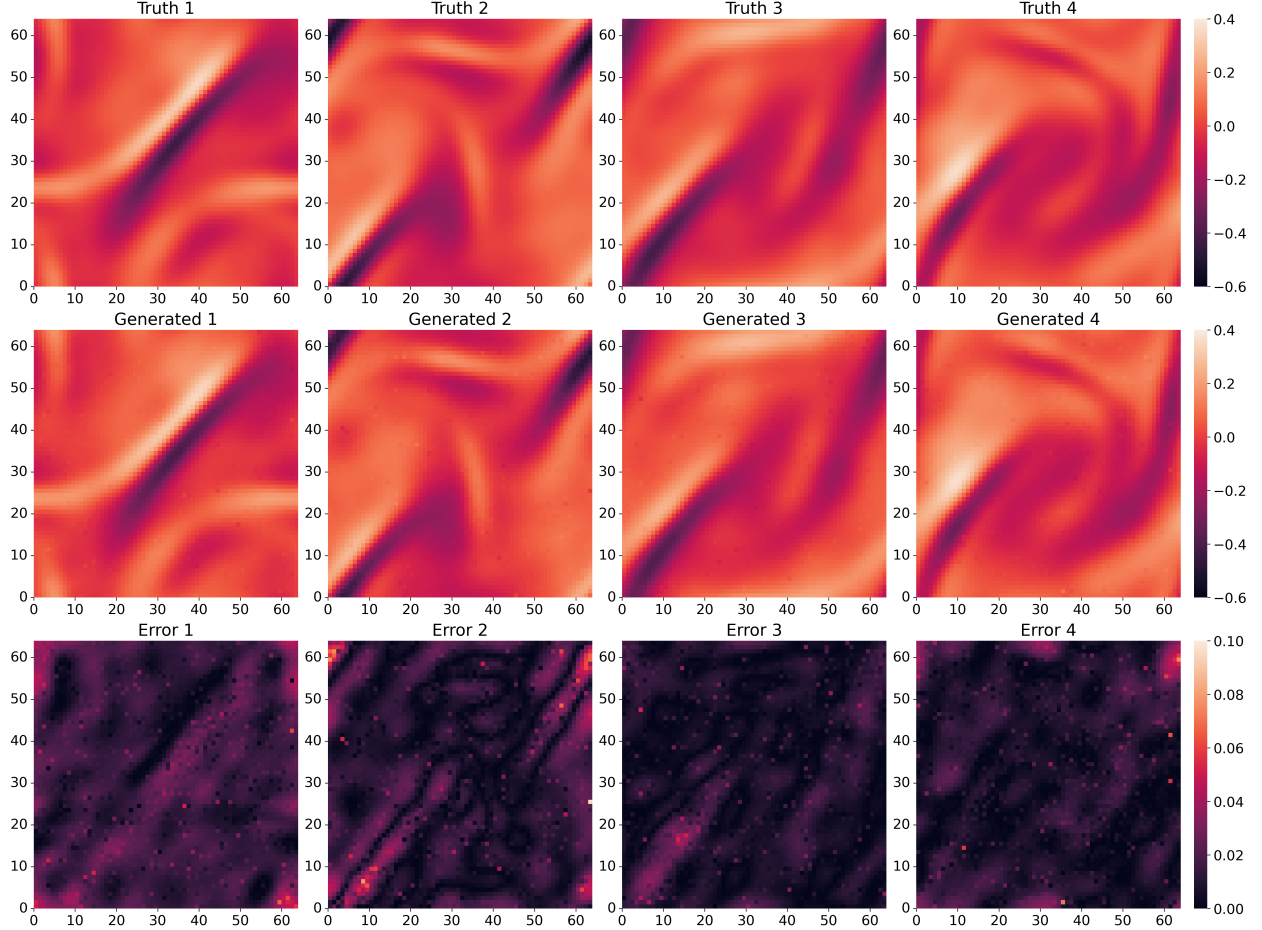


Figure 4: Generated $G(x, t)$ conditioned on current vorticity ω and sparse information of $G_{\text{sparse}}^\dagger$. Sparse information is upsampled using 2-D convolution. Training data resolution: 64×64 . Test data resolution: 64×64 . First row: random samples of the ground truth G^\dagger . Second row: corresponding generated samples G . Third row: absolute error fields between the ground truth G^\dagger and generated G .

Table 2: Errors of the generated G for test data with a resolution of 64×64 . The first row presents the errors when the model is not conditioned on any sparse information $G_{\text{sparse}}^\dagger$. The second row presents the errors when the model is conditioned on bicubically interpolated sparse observations. The third row presents the errors when the model is conditioned on sparsely observed data processed with 2-D convolution.

Methods \ Errors	Test Data		Test Errors	
	dx	dy	D_{MSE}	D_{RE}
No sparse	1/64	1/64	2.9423e-03	0.4316
Interpolation	1/64	1/64	1.1013e-04	0.0835
Convolution	1/64	1/64	1.1648e-04	0.0856

3.2. Resolution Invariance of the Trained Model

To confirm that resolution invariance has been achieved by the proposed stochastic modeling framework, Fig. 5 presents the results of the stochastic viscous diffusion terms from the true system and the ones generated by the conditional diffusion model. The model is tested on

finer resolutions (128×128 , 256×256) that are different from the training data resolution (64×64), with the sparse information of G^\dagger (16×16) incorporated using bicubic interpolation. It can be seen in Fig. 5 that the test results at different resolutions still manage to capture the general patterns of the true system, at least qualitatively.

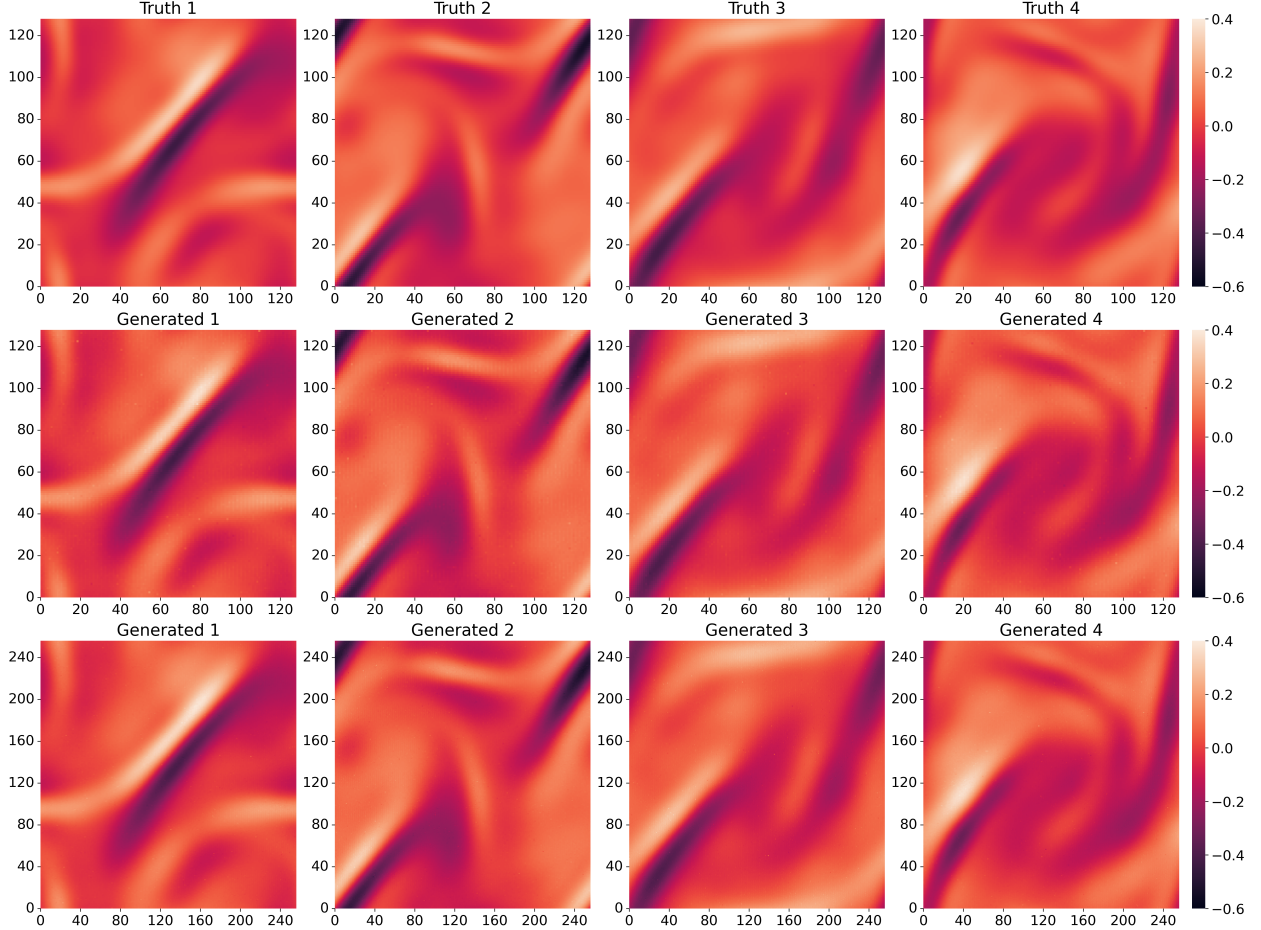


Figure 5: Generated $G(x, t)$ conditioned on current vorticity ω and sparse information of $G_{\text{sparse}}^\dagger$. Sparse information is upscaled using bicubic interpolation. Training data resolution: 64×64 . Test data resolution: 128×128 and 256×256 . First row: random samples of the ground truth $G^\dagger|_{128 \times 128}$. The ground truth $G^\dagger|_{256 \times 256}$ is visually identical hence omitted. Second row: corresponding generated samples $G|_{128 \times 128}$. Third row: corresponding generated samples $G|_{256 \times 256}$.

In Fig. 6, we present results of utilizing 2-D convolution to preprocess sparse information. Kernel size of the 2-D convolution layers to preprocess the sparse information scales with different target resolutions, i.e., for a target of 64×64 , we use a kernel size of 7, while for 128×128 and 256×256 , we use 15 and 31 respectively. Similar to the results in Fig. 5, it can be seen in Fig. 6 that the test results at different resolutions show a good agreement with the true system, which demonstrates that the resolution invariance property of the trained model is not sensitive to the specific technique for upscaling the sparse conditional information.

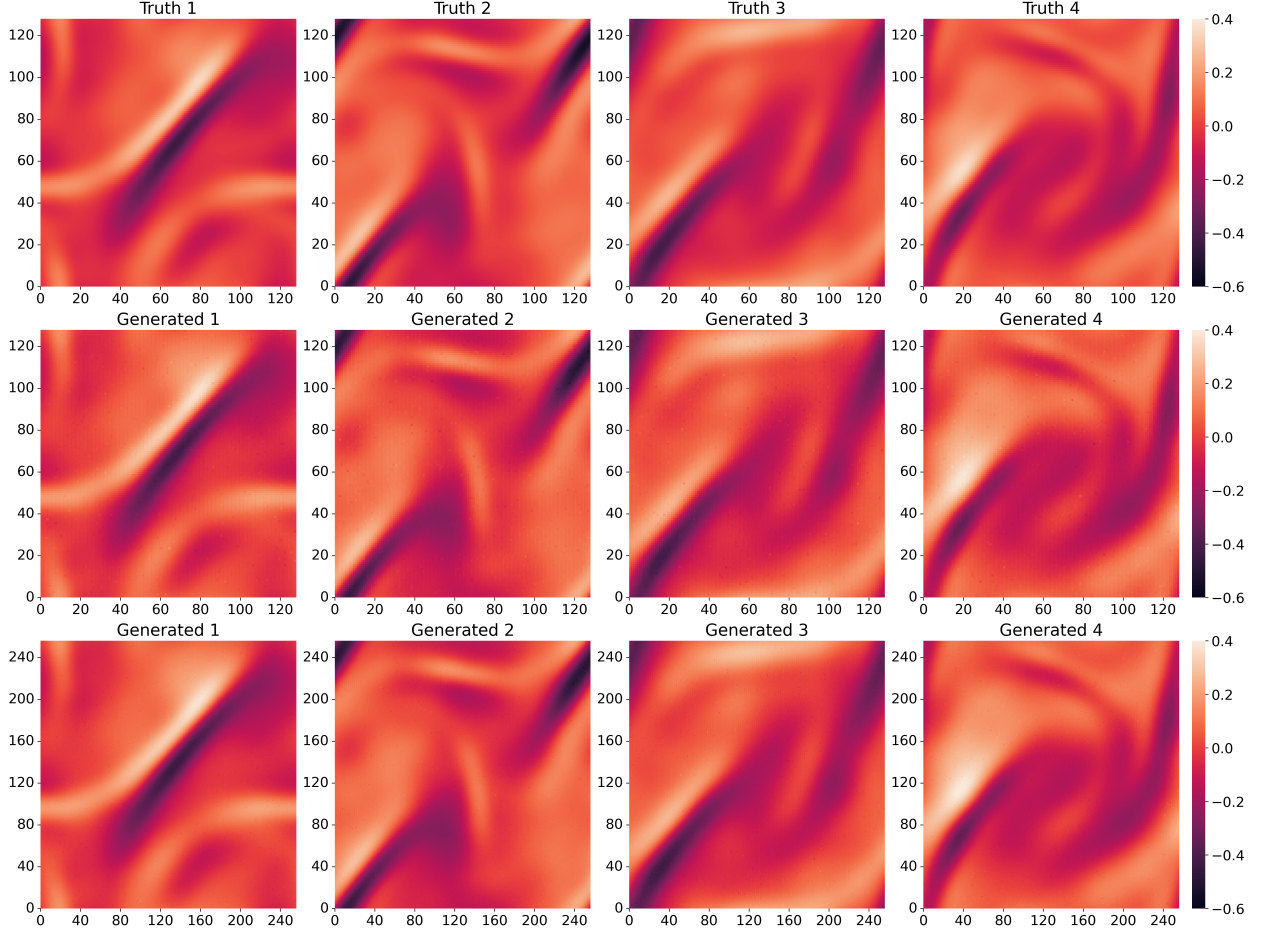


Figure 6: Generated $G(x, t)$ conditioned on current vorticity ω and sparse information of $G_{\text{sparse}}^{\dagger}$. Sparse information is upscaled using 2-D convolution. Training data resolution: 64×64 . Test data resolution: 128×128 and 256×256 . First row: random samples of the ground truth $G^{\dagger}|_{128 \times 128}$. The ground truth $G^{\dagger}|_{256 \times 256}$ is visually identical hence omitted. Second row: corresponding generated samples $G|_{128 \times 128}$. Third row: corresponding generated samples $G|_{256 \times 256}$.

In Table 3, we present quantitative results that further confirm the resolution invariance of our model. Recall that all models were trained on a resolution of 64×64 and tested on different resolutions (64×64 , 128×128 , and 256×256), the results show no significant drop in performance when testing on finer resolutions, demonstrating the robustness of our approach across different resolutions. The main reason for this resolution invariance property of our approach is the use of FNOs to construct the score function with multimodal inputs.

Table 3: Errors of the generated G for test data with different resolutions of 64×64 , 128×128 , and 256×256 . The training resolution is 64×64 . The first to third rows present the errors when the model is conditioned on bicubically interpolated sparse observations, whereas the fourth to sixth rows present the errors when the model is conditioned on sparsely observed data processed with 2-D convolution.

Methods	Errors		Test Errors	
	dx	dy	D_{MSE}	D_{RE}
Interpolation	1/64	1/64	1.1013e-04	0.0835
	1/128	1/128	2.2908e-04	0.1125
	1/256	1/256	3.9921e-04	0.1623
Convolution	1/64	1/64	1.1648e-04	0.0856
	1/128	1/128	1.8334e-04	0.1084
	1/256	1/256	2.8142e-04	0.1247

Figure 7 demonstrates that the generated $G(x, t)$ fields, whether conditioned on interpolated or convoluted sparse information, exhibit a good agreement with the ground truth $G^\dagger(x, t)$ in terms of energy spectra defined in Eq. (23). This indicates that the model performs well and that both techniques for incorporating sparse information are effective. Additionally, the energy spectra calculated from $G^\dagger(x, t)$ at different resolutions also align closely with one another, suggesting that the proposed conditional score-based model successfully achieves resolution invariance. The main reason for the differences between the true system and the model ones in the range of high wave numbers is that the training resolution is only 64×64 , and it is expected that the test results are consistent with the training resolution with lower wave numbers and would not be able to capture the energy spectrum of the true system at higher wave numbers, even with a higher test resolution.

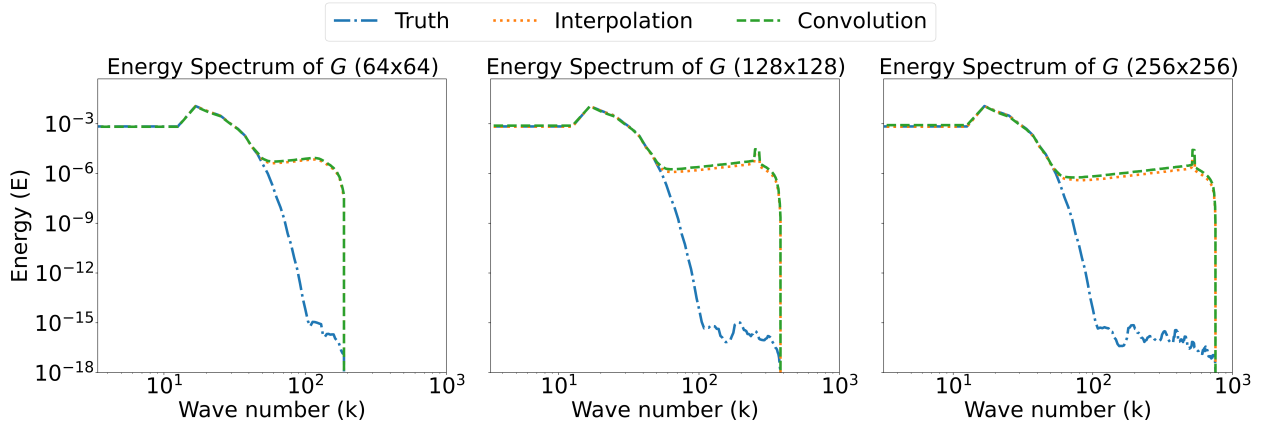


Figure 7: Energy spectrum of the generated G with different test resolutions (64×64 , 128×128 , and 256×256).

3.3. Numerical Simulations of the Vorticity using the Trained Model

The trained score-based model can be used as a surrogate closure model for characterizing the difference between the true system in Eq. (1) and the modeled system in Eq. (2). In this section, we consider the stochastic 2-D Navier-Stokes in Eq. (20) as an example. To simulate the vorticity fields $\omega(x, t)$, we use the same pseudo-spectral and Crank-Nicolson methods for

the data generation process described in [Appendix B](#). For surrogate modeling, recall that our model is trained to conditionally generate the stochastic viscous diffusion term denoted as $G^\dagger(\mathbf{x}, t) = \nu \nabla^2 \omega^\dagger(\mathbf{x}, t) + 2\beta\xi$, we also assume some known information:

- Initial vorticity of the true system: $\omega^\dagger(\mathbf{x}, t_0)$.
- Deterministic forcing: $f(\mathbf{x}) = 0.1(\sin(2\pi(x + y)) + \cos(2\pi(x + y)))$.

The FNO-based score function $s_\theta(\tau, G_\tau, \omega, G_{\text{sparse}}^\dagger)$ is trained based on the details described in the previous section, which approximates true score function $\nabla_G \log p(G(\mathbf{x}, t))$ in the sampling process of $G(\mathbf{x}, t)$ via the proposed score-based conditional diffusion model. We start with $t_0 = 30$ and aim to simulate the vorticity $\omega(\mathbf{x}, t)$ for $t \in [30, 50]$ with a time step of $\Delta t = 10^{-3}$. [Figure 8](#) presents the simulation results neglecting the ground truth G^\dagger and with G generated by the score-based conditional diffusion model. It can be seen that the simulation results without G^\dagger term show noticeable differences from the true system, and a much better agreement with the true system is achieved by the simulation with G term generated by the score-based conditional diffusion model.

It is worth noting that the computational cost can be infeasible for performing full reverse SDE sampling at every step of the Crank-Nicolson update in the numerical simulation of the modeled system. To address this issue and improve efficiency, we first speed up the generation process by starting from a prior distribution that is closer to the ground truth data distribution (i.e., a smaller T for the reverse SDE) and using an adaptive scheme for step sizes, as both discussed in [Section 2.3](#). Additionally, improving efficiency while maintaining acceptable error levels can be achieved through sub-sampling the numerical scheme. Specifically, we can perform one instance of reverse SDE sampling every n steps of the Crank-Nicolson update while n is a tunable parameter. For the simulation results with G^\dagger term in [Fig. 8](#), we initiate the reverse SDE at $T = 0.1$, use 10 adaptive time steps based on the scheduling function in [Eq. \(19\)](#), and perform reverse SDE sampling every 5 steps of the Crank-Nicolson update. For $G(\mathbf{x}, t)$ in the intervening steps of the numerical scheme where we opt not to perform reverse SDE sampling, we use an approximation of $G(\mathbf{x}, t_n + \Delta t) = G(\mathbf{x}, t_n) + \beta z$, where $z \sim \mathcal{N}(0, I)$ and $\beta = 5 \times 10^{-5}$ is the same noise scale coefficient used in the original 2-D Navier-Stokes equation.

[Table 4](#) summarizes the performances and computational costs across four different simulation settings. Simulation I corresponds to the simulated ω when G^\dagger is completely removed, which leads to much larger errors than the other three simulation settings. Simulation II corresponds to the one that utilizes all the speedup techniques introduced above. Simulation III is designed to have similar computational costs as Simulation II. It starts each reverse SDE solving at $T = 0.1$ but utilizes 10 fixed-size time steps, producing less accurate generation of G and subsequently leading to larger errors of ω than Simulation II, which has adaptive time steps for the reverse SDE. Simulation IV, serving as the baseline method, shows the best accuracy but incurs the highest computational cost due to performing reverse SDE generation at every simulation step, with denoising initiated at $T = 1$ and redundant 1000 fixed-size time steps for each sampling process. [Figure 9](#) illustrates the error comparison of the numerical simulations that deploy a score-based generative closure term with different sampling

strategies, which corresponds to Simulation II, III, and IV. With the costs in Table 4 and the errors in Fig. 9, we can see that Simulation II provides a good balance between accuracy and simulation cost, confirming the effectiveness of the proposed fast sampling strategy for deploying diffusion models as stochastic data-driven closure terms in numerical simulations.

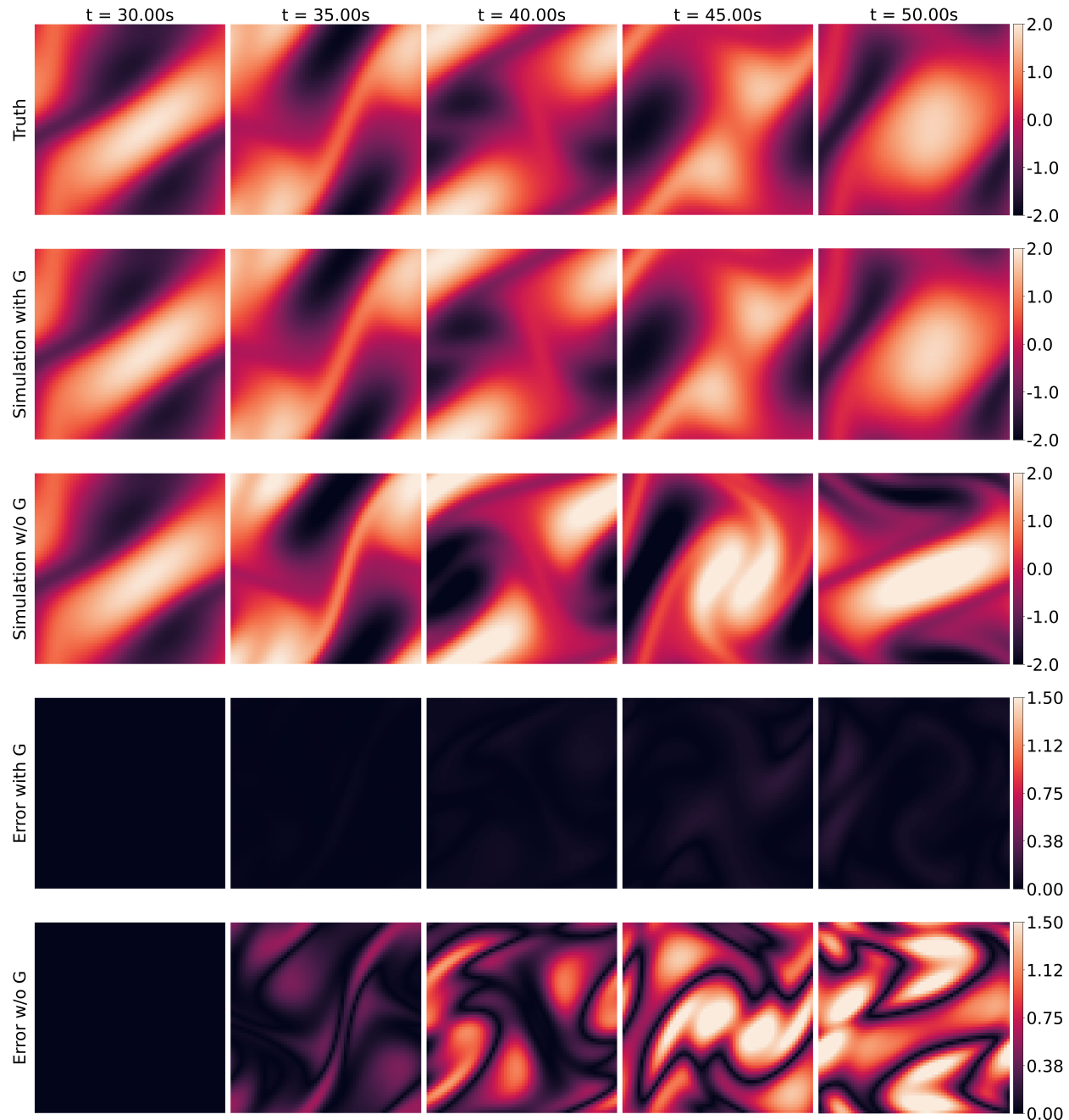


Figure 8: Numerical simulation results of vorticity ω from 30s to 50s using trained conditional score-based model. Sparse information is upscaled via 2-D convolution. First row: the ground truth vorticity ω^\dagger at various times. Second row: corresponding simulated ω with generated G . Third row: corresponding simulated ω with G^\dagger neglected. Fourth row: absolute error fields between the ground truth of vorticity ω^\dagger and the simulated ω with G . Fifth row: absolute error fields between ω^\dagger and the simulated ω without G^\dagger .

Table 4: A comparison of computational cost, accuracy of generated G terms, and accuracy of simulated vorticity ω from 30s - 50s. The index I corresponds to the simulation of ω with G^\dagger term neglected. II corresponds to the simulation with generated G term every 5 physical time steps, and for each generated sample, the denoising process starts at $\tau = 0.1$ using 10 time steps with adaptive sizes. III corresponds to the simulation with generated G term every 5 physical time steps, and for each generation, the denoising process starts at $\tau = 0.1$ using 10 time steps with fixed sizes. IV corresponds to the generated G term at each physical time step, and for each generation, the denoising process starts at $\tau = 1$ using 1000 time steps with a fixed size.

Simulations	Costs	Errors	Generated G	$\omega(t = 30)$	$\omega(t = 35)$	$\omega(t = 40)$	$\omega(t = 45)$	$\omega(t = 50)$
I	17.4	D_{RE}	NA	0	5.9232e-02	3.0145e-01	7.1893e-01	8.5814e-01
		D_{MSE}	NA	0	0.2431	0.5771	0.9246	1.0315
II	266.2	D_{RE}	1.4214e-04	0	1.2402e-04	1.3887e-03	3.3429e-03	3.1497e-03
		D_{MSE}	0.0945	0	0.0111	0.0392	0.0631	0.0625
III	269.8	D_{RE}	2.1703e-03	0	1.3740e-04	1.5141e-03	3.8441e-03	3.6798e-03
		D_{MSE}	0.3829	0	0.0117	0.0409	0.0676	0.0675
IV	81425.2	D_{RE}	1.2152e-04	0	1.2028e-04	1.2698e-03	2.7910e-03	2.7792e-03
		D_{MSE}	0.0881	0	0.0110	0.0375	0.0576	0.0587

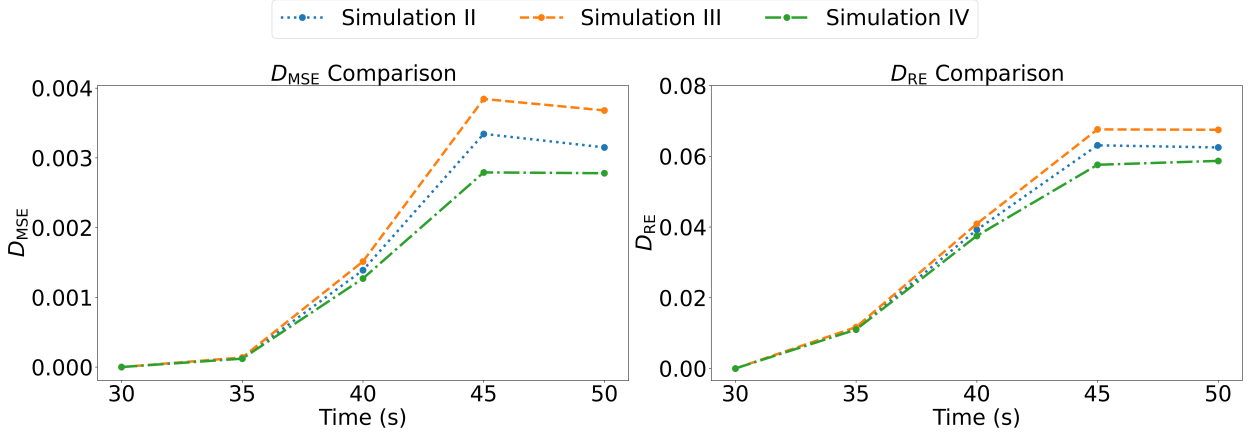


Figure 9: A comparison for the accuracy of simulated vorticity ω from 30s to 50s with different simulation settings.

4. Conclusions

Many complex dynamical systems are featured by a wide range of scales, such as turbulence or the earth system, for which numerically resolving all the scales is still infeasible in the foreseeable future. Closure models are thus needed to characterize the impact of unresolved scales on the resolved ones. In this work, we present a data-driven modeling framework to build stochastic and non-local closure models based on the conditional diffusion model and neural operator. More specifically, the Fourier neural operator is used to approximate the score function for a score-based generative diffusion model, which captures the conditional probability distribution of the unknown closure term given some dependent information, e.g., the numerically resolved scales of the true system, sparse experimental measurements of the true closure term, and estimation of the closure term from existing physics-based models. Fast sampling algorithms are also investigated to ensure the efficiency of the proposed framework. A comprehensive study is performed on the 2-D Navier–Stokes equation,

for which the stochastic viscous diffusion term is assumed to be unknown. Results show that (i) conditioning on dependent information can help achieve a good performance of the diffusion-model-based closure with a limited amount of training data and (ii) employing a neural operator to approximate the score function can help achieve the resolution invariance of the trained model. The proposed framework provides a systematic data-driven approach to building and calibrating stochastic and non-local closure models for some challenging science and engineering applications that lack a scale separation between resolved and unresolved scales, for which deterministic and local closure models are not sophisticated enough to provide a generalizable model that characterizes the contribution of unresolved scales to the resolved ones.

Acknowledgments

X.D., C.C. and J.W. are supported by the University of Wisconsin-Madison, Office of the Vice Chancellor for Research and Graduate Education with funding from the Wisconsin Alumni Research Foundation.

References

- [1] P. Moin, K. Mahesh, Direct numerical simulation: a tool in turbulence research, *Annual Review of Fluid Mechanics* 30 (1998) 539–578.
- [2] B. E. Launder, D. B. Spalding, The numerical computation of turbulent flows, in: *Numerical Prediction of Flow, Heat Transfer, Turbulence and Combustion*, Elsevier, 1983, pp. 96–116.
- [3] D. C. Wilcox, et al., *Turbulence Modeling for CFD*, volume 2, DCW Industries La Canada, CA, 1998.
- [4] J. Smagorinsky, General circulation experiments with the primitive equations: I. the basic experiment, *Monthly Weather Review* 91 (1963) 99–164.
- [5] J. W. Deardorff, A numerical study of three-dimensional turbulent channel flow at large Reynolds numbers, *Journal of Fluid Mechanics* 41 (1970) 453–480.
- [6] R. Zwanzig, *Nonequilibrium Statistical Mechanics*, Oxford University Press, 2001.
- [7] V. Lucarini, R. Blender, C. Herbert, F. Ragone, S. Pascale, J. Wouters, Mathematical and physical ideas for climate science, *Rev. Geophys.* 52 (2014) 809–859.
- [8] A. J. Chorin, F. Lu, Discrete approach to stochastic parametrization and dimension reduction in nonlinear dynamics, *Proceedings of the National Academy of Sciences* 112 (2015) 9804–9809.
- [9] C. L. Franzke, T. J. O’Kane, J. Berner, P. D. Williams, V. Lucarini, *Stochastic climate theory and modeling*, *Wiley Interdisciplinary Reviews: Climate Change* 6 (2015) 63–78.
- [10] F. Lu, K. K. Lin, A. J. Chorin, Data-based stochastic model reduction for the Kuramoto–Sivashinsky equation, *Physica D: Nonlinear Phenomena* 340 (2017) 46–57.

- [11] T. Palmer, Stochastic weather and climate models, *Nature Reviews Physics* 1 (2019) 463–471.
- [12] T. Schneider, A. M. Stuart, J.-L. Wu, Learning stochastic closures using ensemble Kalman inversion, *Transactions of Mathematics and Its Applications* 5 (2021) ttab003.
- [13] N. Chen, *Stochastic Methods for Modeling and Predicting Complex Dynamical Systems: Uncertainty Quantification, State Estimation, and Reduced-Order Models*, Springer Nature, 2023.
- [14] N. Chen, X. Fang, A simple multiscale intermediate coupled stochastic model for El Niño diversity and complexity, *Journal of Advances in Modeling Earth Systems* 15 (2023) e2022MS003469.
- [15] J.-L. Wu, M. E. Levine, T. Schneider, A. Stuart, Learning about structural errors in models of complex dynamical systems, *Journal of Computational Physics* (2024) 113157.
- [16] S. L. Brunton, J. L. Proctor, J. N. Kutz, Discovering governing equations from data by sparse identification of nonlinear dynamical systems, *Proceedings of the National Academy of Sciences* 113 (2016) 3932–3937.
- [17] J.-X. Wang, J.-L. Wu, H. Xiao, Physics-informed machine learning approach for reconstructing reynolds stress modeling discrepancies based on DNS data, *Physical Review Fluids* 2 (2017) 034603.
- [18] J.-L. Wu, H. Xiao, E. Paterson, Physics-informed machine learning approach for augmenting turbulence models: A comprehensive framework, *Physical Review Fluids* 3 (2018) 074602.
- [19] R. Maulik, O. San, A. Rasheed, P. Vedula, Subgrid modelling for two-dimensional turbulence using neural networks, *Journal of Fluid Mechanics* 858 (2019) 122–144.
- [20] K. Duraisamy, G. Iaccarino, H. Xiao, Turbulence modeling in the age of data, *Annual Review of Fluid Mechanics* 51 (2019) 357–377.
- [21] K. Kashinath, M. Mustafa, A. Albert, J. Wu, C. Jiang, S. Esmailzadeh, K. Aziz-zadenesheli, R. Wang, A. Chattopadhyay, A. Singh, et al., Physics-informed machine learning: case studies for weather and climate modelling, *Philosophical Transactions of the Royal Society A* 379 (2021) 20200093.
- [22] A. Gupta, P. F. Lermusiaux, Neural closure models for dynamical systems, *Proceedings of the Royal Society A* 477 (2021) 20201004.
- [23] R. Vinuesa, S. L. Brunton, Enhancing computational fluid dynamics with machine learning, *Nature Computational Science* 2 (2022) 358–366.
- [24] A. Gupta, P. F. Lermusiaux, Generalized neural closure models with interpretability, *Scientific Reports* 13 (2023) 10634.

- [25] C. Chen, N. Chen, J.-L. Wu, CEBoosting: Online sparse identification of dynamical systems with regime switching by causation entropy boosting, *Chaos: An Interdisciplinary Journal of Nonlinear Science* 33 (2023).
- [26] C. Chen, J.-L. Wu, Operator learning for continuous spatial-temporal model with a hybrid optimization scheme, arXiv preprint arXiv:2311.11798 (2023).
- [27] C. Chen, N. Chen, J.-L. Wu, CGNSDE: Conditional Gaussian neural stochastic differential equation for modeling complex systems and data assimilation, *Computer Physics Communications* 304 (2024) 109302.
- [28] P. Stinis, T. Hagge, A. M. Tartakovsky, E. Yeung, Enforcing constraints for interpolation and extrapolation in generative adversarial networks, *Journal of Computational Physics* 397 (2019) 108844.
- [29] J.-L. Wu, K. Kashinath, A. Albert, D. Chirila, H. Xiao, et al., Enforcing statistical constraints in generative adversarial networks for modeling chaotic dynamical systems, *Journal of Computational Physics* 406 (2020) 109209.
- [30] L. Yang, D. Zhang, G. E. Karniadakis, Physics-informed generative adversarial networks for stochastic differential equations, *SIAM Journal on Scientific Computing* 42 (2020) A292–A317.
- [31] M. Cheng, F. Fang, C. C. Pain, I. Navon, Data-driven modelling of nonlinear spatio-temporal fluid flows using a deep convolutional generative adversarial network, *Computer Methods in Applied Mechanics and Engineering* 365 (2020) 113000.
- [32] P. Perezhogin, L. Zanna, C. Fernandez-Granda, Generative data-driven approaches for stochastic subgrid parameterizations in an idealized ocean model, *Journal of Advances in Modeling Earth Systems* 15 (2023) e2023MS003681.
- [33] J. Ho, A. Jain, P. Abbeel, Denoising diffusion probabilistic models, *Advances in Neural Information Processing Systems* 33 (2020) 6840–6851.
- [34] J. Sohl-Dickstein, E. Weiss, N. Maheswaranathan, S. Ganguli, Deep unsupervised learning using nonequilibrium thermodynamics, in: *International Conference on Machine Learning*, PMLR, 2015, pp. 2256–2265.
- [35] P. Dhariwal, A. Nichol, Diffusion models beat GANs on image synthesis, *Advances in Neural Information Processing Systems* 34 (2021) 8780–8794.
- [36] Y. Song, S. Ermon, Generative modeling by estimating gradients of the data distribution, *Advances in Neural Information Processing Systems* 32 (2019).
- [37] Y. Song, J. Sohl-Dickstein, D. P. Kingma, A. Kumar, S. Ermon, B. Poole, Score-based generative modeling through stochastic differential equations, *International Conference on Learning Representations* (2021).

- [38] A. Hyvärinen, P. Dayan, Estimation of non-normalized statistical models by score matching, *Journal of Machine Learning Research* 6 (2005).
- [39] P. Vincent, A connection between score matching and denoising autoencoders, *Neural Computation* 23 (2011) 1661–1674.
- [40] J. Song, C. Meng, S. Ermon, Denoising diffusion implicit models, in: *International Conference on Learning Representations*, 2021.
- [41] C.-W. Huang, J. H. Lim, A. C. Courville, A variational perspective on diffusion-based generative models and score matching, *Advances in Neural Information Processing Systems* 34 (2021) 22863–22876.
- [42] D. P. Kingma, M. Welling, Auto-encoding variational Bayes, *arXiv preprint arXiv:1312.6114* (2013).
- [43] I. Goodfellow, J. Pouget-Abadie, M. Mirza, B. Xu, D. Warde-Farley, S. Ozair, A. Courville, Y. Bengio, Generative adversarial nets, *Advances in Neural Information Processing Systems* 27 (2014).
- [44] C. Saharia, W. Chan, H. Chang, C. Lee, J. Ho, T. Salimans, D. Fleet, M. Norouzi, Palette: Image-to-image diffusion models, in: *ACM SIGGRAPH 2022 Conference Proceedings*, 2022, pp. 1–10.
- [45] R. Rombach, A. Blattmann, D. Lorenz, P. Esser, B. Ommer, High-resolution image synthesis with latent diffusion models, in: *Proceedings of the IEEE/CVF Conference on Computer Vision and Pattern Recognition*, 2022, pp. 10684–10695.
- [46] J. Ho, T. Salimans, Classifier-free diffusion guidance, in: *NeurIPS 2021 Workshop on Deep Generative Models and Downstream Applications*, 2021.
- [47] Y. Tashiro, J. Song, Y. Song, S. Ermon, CSDI: Conditional score-based diffusion models for probabilistic time series imputation, *Advances in Neural Information Processing Systems* 34 (2021) 24804–24816.
- [48] K. Rasul, C. Seward, I. Schuster, R. Vollgraf, Autoregressive denoising diffusion models for multivariate probabilistic time series forecasting, in: *International Conference on Machine Learning*, PMLR, 2021, pp. 8857–8868.
- [49] H. Wen, Y. Lin, Y. Xia, H. Wan, Q. Wen, R. Zimmermann, Y. Liang, DiffSTG: Probabilistic spatio-temporal graph forecasting with denoising diffusion models, in: *Proceedings of the 31st ACM International Conference on Advances in Geographic Information Systems*, 2023, pp. 1–12.
- [50] G. Yang, S. Sommer, A denoising diffusion model for fluid field prediction, *arXiv preprint arXiv:2301.11661* (2023).
- [51] T. Li, L. Biferale, F. Bonaccorso, M. A. Scarpolini, M. Buzzicotti, Synthetic Lagrangian turbulence by generative diffusion models, *Nature Machine Intelligence* (2024) 1–11.

- [52] P. Lippe, B. Veeling, P. Perdikaris, R. Turner, J. Brandstetter, PDE-refiner: Achieving accurate long rollouts with neural PDE solvers, *Advances in Neural Information Processing Systems* 36 (2024).
- [53] D. Shu, Z. Li, A. B. Farimani, A physics-informed diffusion model for high-fidelity flow field reconstruction, *Journal of Computational Physics* 478 (2023) 111972.
- [54] H. Gao, X. Han, X. Fan, L. Sun, L.-P. Liu, L. Duan, J.-X. Wang, Bayesian conditional diffusion models for versatile spatiotemporal turbulence generation, *Computer Methods in Applied Mechanics and Engineering* 427 (2024) 117023.
- [55] C. Jacobsen, Y. Zhuang, K. Duraisamy, Cocogen: physically-consistent and conditioned score-based generative models for forward and inverse problems, *arXiv preprint arXiv:2312.10527* (2023).
- [56] J. Qiu, J. Huang, X. Zhang, Z. Lin, M. Pan, Z. Liu, F. Miao, Pi-fusion: Physics-informed diffusion model for learning fluid dynamics, *arXiv preprint arXiv:2406.03711* (2024).
- [57] J.-H. Bastek, W. Sun, D. M. Kochmann, Physics-informed diffusion models, *arXiv preprint arXiv:2403.14404* (2024).
- [58] T. Salimans, J. Ho, Progressive distillation for fast sampling of diffusion models, in: *International Conference on Learning Representations*, 2022.
- [59] Y. Song, P. Dhariwal, M. Chen, I. Sutskever, Consistency models, in: *Proceedings of the 40th International Conference on Machine Learning, ICML'23, JMLR.org*, 2023.
- [60] C. Meng, R. Rombach, R. Gao, D. Kingma, S. Ermon, J. Ho, T. Salimans, On distillation of guided diffusion models, in: *Proceedings of the IEEE/CVF Conference on Computer Vision and Pattern Recognition*, 2023, pp. 14297–14306.
- [61] A. Jolicoeur-Martineau, K. Li, R. Piché-Taillefer, T. Kachman, I. Mitliagkas, Gotta go fast when generating data with score-based models, *arXiv preprint arXiv:2105.14080* (2021).
- [62] T. Karras, M. Aittala, T. Aila, S. Laine, Elucidating the design space of diffusion-based generative models, *Advances in Neural Information Processing Systems* 35 (2022) 26565–26577.
- [63] L. Lu, P. Jin, G. Pang, Z. Zhang, G. E. Karniadakis, Learning nonlinear operators via deepoNet based on the universal approximation theorem of operators, *Nature Machine Intelligence* 3 (2021) 218–229.
- [64] Z. Li, N. B. Kovachki, K. Azizzadenesheli, B. liu, K. Bhattacharya, A. Stuart, A. Anandkumar, Fourier neural operator for parametric partial differential equations, in: *International Conference on Learning Representations*, 2021.

- [65] N. Kovachki, Z. Li, B. Liu, K. Azizzadenesheli, K. Bhattacharya, A. Stuart, A. Anandkumar, Neural operator: Learning maps between function spaces with applications to pdes, *Journal of Machine Learning Research* 24 (2023) 1–97.
- [66] A. Tran, A. Mathews, L. Xie, C. S. Ong, Factorized fourier neural operators, in: *The Eleventh International Conference on Learning Representations*, 2023.
- [67] S. Goswami, M. Yin, Y. Yu, G. E. Karniadakis, A physics-informed variational DeepONet for predicting crack path in quasi-brittle materials, *Computer Methods in Applied Mechanics and Engineering* 391 (2022) 114587.
- [68] G. Wen, Z. Li, K. Azizzadenesheli, A. Anandkumar, S. M. Benson, U-FNO—an enhanced fourier neural operator-based deep-learning model for multiphase flow, *Advances in Water Resources* 163 (2022) 104180.
- [69] Z. Li, D. Z. Huang, B. Liu, A. Anandkumar, Fourier neural operator with learned deformations for PDEs on general geometries, *Journal of Machine Learning Research* 24 (2023) 1–26.
- [70] K. Chwialkowski, H. Strathmann, A. Gretton, A kernel test of goodness of fit, in: *International Conference on Machine Learning*, PMLR, 2016, pp. 2606–2615.
- [71] Q. Liu, J. Lee, M. Jordan, A kernelized stein discrepancy for goodness-of-fit tests, in: *International Conference on Machine Learning*, PMLR, 2016, pp. 276–284.
- [72] Y. Song, S. Garg, J. Shi, S. Ermon, Sliced score matching: A scalable approach to density and score estimation, in: *Uncertainty in Artificial Intelligence*, PMLR, 2020, pp. 574–584.
- [73] G. Parisi, Correlation functions and computer simulations, *Nuclear Physics B* 180 (1981) 378–384.
- [74] U. Grenander, M. I. Miller, Representations of knowledge in complex systems, *Journal of the Royal Statistical Society: Series B (Methodological)* 56 (1994) 549–581.
- [75] B. D. Anderson, Reverse-time diffusion equation models, *Stochastic Processes and their Applications* 12 (1982) 313–326.
- [76] Q. Du, M. Gunzburger, R. B. Lehoucq, K. Zhou, Analysis and approximation of nonlocal diffusion problems with volume constraints, *SIAM Review* 54 (2012) 667–696.
- [77] M. D’Elia, Q. Du, C. Glusa, M. Gunzburger, X. Tian, Z. Zhou, Numerical methods for nonlocal and fractional models, *Acta Numerica* 29 (2020) 1–124.
- [78] H. You, Y. Yu, N. Trask, M. Gulian, M. D’Elia, Data-driven learning of nonlocal physics from high-fidelity synthetic data, *Computer Methods in Applied Mechanics and Engineering* 374 (2021) 113553.
- [79] C. Ma, J. Wang, E. Weinan, Model reduction with memory and the machine learning of dynamical systems, *Communications in Computational Physics* 25 (2019) 947–962.

- [80] Q. Wang, N. Ripamonti, J. S. Hesthaven, Recurrent neural network closure of parametric pod-galerkin reduced-order models based on the Mori-Zwanzig formalism, *Journal of Computational Physics* 410 (2020) 109402.
- [81] K. K. Lin, F. Lu, Data-driven model reduction, Wiener projections, and the Koopman-Mori-Zwanzig formalism, *Journal of Computational Physics* 424 (2021) 109864.
- [82] A.-T. G. Charalampopoulos, T. P. Sapsis, Machine-learning energy-preserving nonlocal closures for turbulent fluid flows and inertial tracers, *Physical Review Fluids* 7 (2022) 024305.
- [83] M. Tancik, P. Srinivasan, B. Mildenhall, S. Fridovich-Keil, N. Raghavan, U. Singhal, R. Ramamoorthi, J. Barron, R. Ng, Fourier features let networks learn high frequency functions in low dimensional domains, *Advances in Neural Information Processing Systems* 33 (2020) 7537–7547.

Appendix A. Objective Functions of Score Matching

Appendix A.1. Equivalency between ESM and DSM

In this appendix, we first prove that the explicit score matching (ESM) and the denoising score matching (DSM) have equivalent objectives. Let us consider the explicit score matching which has an objective function

$$\begin{aligned} J_{\text{ESM}}(\theta) &= \mathbb{E}_{U_\tau \sim p(U_\tau)} \|\nabla_{U_\tau} \log p(U_\tau) - s_\theta(\tau, U_\tau)\|_2^2 \\ &= \mathbb{E}_{U_\tau \sim p(U_\tau)} \|s_\theta(\tau, U_\tau)\|_2^2 - 2H(\theta) + C_1 \end{aligned} \quad (\text{A.1})$$

where $C_1 = \mathbb{E}_{U_\tau \sim p(U_\tau)} \|\nabla_{U_\tau} \log p(U_\tau)\|_2^2$ is a constant that does not depend on model parameters θ .

For $H(\theta)$, we have

$$\begin{aligned} H(\theta) &= \mathbb{E}_{U_\tau \sim p(U_\tau)} [\langle \nabla_{U_\tau} \log p(U_\tau), s_\theta(\tau, U_\tau) \rangle] \\ &= \int_{U_\tau} p(U_\tau) \langle \nabla_{U_\tau} \log p(U_\tau), s_\theta(\tau, U_\tau) \rangle dU_\tau \\ &= \int_{U_\tau} p(U_\tau) \left\langle \frac{\nabla_{U_\tau} p(U_\tau)}{p(U_\tau)}, s_\theta(\tau, U_\tau) \right\rangle dU_\tau \\ &= \int_{U_\tau} \langle \nabla_{U_\tau} p(U_\tau), s_\theta(\tau, U_\tau) \rangle dU_\tau \\ &= \int_{U_\tau} \left\langle \nabla_{U_\tau} \int_{U_0} p(U_0) p(U_\tau | U_0) dU_0, s_\theta(\tau, U_\tau) \right\rangle dU_\tau \\ &= \int_{U_\tau} \left\langle \int_{U_0} p(U_0) \nabla_{U_\tau} p(U_\tau | U_0) dU_0, s_\theta(\tau, U_\tau) \right\rangle dU_\tau \\ &= \int_{U_\tau} \left\langle \int_{U_0} p(U_0) p(U_\tau | U_0) \nabla_{U_\tau} \log p(U_\tau | U_0) dU_0, s_\theta(\tau, U_\tau) \right\rangle dU_\tau \\ &= \int_{U_\tau} \int_{U_0} p(U_0) p(U_\tau | U_0) \langle \nabla_{U_\tau} \log p(U_\tau | U_0), s_\theta(\tau, U_\tau) \rangle dU_0 dU_\tau \\ &= \int_{U_\tau} \int_{U_0} p(U_\tau, U_0) \langle \nabla_{U_\tau} \log p(U_\tau | U_0), s_\theta(\tau, U_\tau) \rangle dU_0 dU_\tau \\ &= \mathbb{E}_{U_\tau \sim p(U_\tau | U_0)} \mathbb{E}_{U_0 \sim p(U_0)} [\langle \nabla_{U_\tau} \log p(U_\tau | U_0), s_\theta(\tau, U_\tau) \rangle]. \end{aligned} \quad (\text{A.2})$$

Substituting this expression for $H(\theta)$ in Eq. (A.1) yields

$$\begin{aligned} J_{\text{ESM}}(\theta) &= \mathbb{E}_{U_\tau \sim p(U_\tau)} \|s_\theta(\tau, U_\tau)\|_2^2 \\ &\quad - 2\mathbb{E}_{U_\tau \sim p(U_\tau | U_0)} \mathbb{E}_{U_0 \sim p(U_0)} [\langle \nabla_{U_\tau} \log p(U_\tau | U_0), s_\theta(\tau, U_\tau) \rangle] + C_1. \end{aligned} \quad (\text{A.3})$$

For the denoising score matching objective mentioned in Eq. (10), we have

$$\begin{aligned} J_{\text{DSM}}(\theta) &= \mathbb{E}_{U_\tau \sim p(U_\tau | U_0)} \mathbb{E}_{U_0 \sim p(U_0)} \|\nabla_{U_\tau} \log p(U_\tau | U_0) - s_\theta(\tau, U_\tau)\|_2^2 \\ &= \mathbb{E}_{U_\tau \sim p(U_\tau | U_0)} \mathbb{E}_{U_0 \sim p(U_0)} \|s_\theta(\tau, U_\tau)\|_2^2 \\ &\quad - 2\mathbb{E}_{U_\tau \sim p(U_\tau | U_0)} \mathbb{E}_{U_0 \sim p(U_0)} [\langle \nabla_{U_\tau} \log p(U_\tau | U_0), s_\theta(\tau, U_\tau) \rangle] + C_2, \end{aligned} \quad (\text{A.4})$$

where $C_2 = \mathbb{E}_{U_\tau \sim p(U_\tau | U_0)} \mathbb{E}_{U_0 \sim p(U_0)} \|\nabla_{U_\tau} \log p(U_\tau | U_0)\|_2^2$ is a constant independent of θ .

Viewing Eq. (A.1) and Eq. (A.4), we notice that

$$J_{\text{ESM}}(\theta) = J_{\text{DSM}}(\theta) + C_1 - C_2. \quad (\text{A.5})$$

Thus, the two objective functions are equivalent, up to a constant.

Appendix A.2. Conditional Score Matching

For modeling the conditional distribution $p(U | y)$, we first recall that the condition score matching objectives build upon the fact that the forward process of diffusion model is a Markov chain, meaning that

$$p(U_\tau | U_0, y) = p(U_\tau | U_0), \quad (\text{A.6})$$

where y denotes the conditions. In this paper, y includes resolved system state V , sparse measurements of true U , and other dependent information.

Then, for the conditional score matching (CSM), we simply need to further marginalize the conditions y and get

$$\begin{aligned} J_{\text{CSM}}(\theta, y) &= \mathbb{E}_{U_\tau \sim p(U_\tau | U_0)} \mathbb{E}_{U_0 \sim p(U_0 | y)} \mathbb{E}_{y \sim p(y)} \|\nabla_{U_\tau} \log p(U_\tau | U_0, y) - s_\theta(\tau, U_\tau, y)\|_2^2 \\ &= \mathbb{E}_{U_\tau \sim p(U_\tau | U_0)} \mathbb{E}_{(U_0, y) \sim p(U_0, y)} \|\nabla_{U_\tau} \log p(U_\tau | U_0) - s_\theta(\tau, U_\tau, y)\|_2^2 \end{aligned} \quad (\text{A.7})$$

Appendix B. Details of the Numerical Solver

The data for the 2-D Navier-Stokes equation in Eq. (20) is generated using the pseudo-spectral method combined with the Crank-Nicolson scheme.

Appendix B.1. Pseudo-Spectral Solver

Start off, we have initial conditions $\omega(x, t_0) \sim \mathcal{N}(0, 7^{3/2}(-\Delta + 49I)^{-5/2})$ with periodic boundary conditions, where Δ is a Laplace operator and I is the identity operator. Operating in the Fourier space, we shall first have

$$\hat{\omega}(k, t_0) = \mathcal{F}(\omega(x, t_0)), \quad (\text{B.1})$$

where \mathcal{F} denotes Fourier transformation, $\hat{\omega}$ denotes the Fourier coefficients of the vorticity field ω , and $k = (k_x, k_y)$ represents wavenumbers which are computed based on the grid size.

To approximate the convection and diffusion term, we start with calculating the Laplacian in Fourier space which is given by a constant

$$C = 4\pi^2(k_x^2 + k_y^2). \quad (\text{B.2})$$

Then the stream function ψ is obtained by solving the Poisson equation in Fourier space

$$\hat{\psi} = \frac{\hat{\omega}}{C}, \quad (\text{B.3})$$

with the velocity fields computed as

$$\hat{u} = \left[(2\pi i k_y) \hat{\psi}, - (2\pi i k_x) \hat{\psi} \right]. \quad (\text{B.4})$$

The gradient of vorticity $\nabla\hat{\omega}$ is also calculated in the Fourier space in a similar fashion as shown in Eq. (B.4). Then, $\nabla\hat{\omega}$ and \hat{u} are converted back to the physical space via inverse Fourier transform to calculate the nonlinear convection term which we denote as

$$F(\mathbf{x}, t) = u(\mathbf{x}, t) \cdot \nabla\omega(\mathbf{x}, t) \quad (\text{B.5})$$

Appendix B.2. Crank-Nicolson Method

The vorticity field is updated at each time step using the Crank-Nicolson scheme, which is implicit in time and second-order accurate:

$$\hat{\omega}(k, t_{n+1}) = \frac{\hat{\omega}(k, t_n) - \Delta t \hat{F}(k, t_n) + \Delta t \hat{f}(k) + \frac{\Delta t}{2} \nu C \hat{\omega}(k, t_n) + \Delta t \beta \hat{\xi}_n}{1 + \frac{\Delta t}{2} \nu C} \quad (\text{B.6})$$

where $\nu = 10^{-3}$ is the viscosity, $\Delta t = 10^{-3}$ is the time step, C is the Laplacian in Fourier space, $\hat{F}(k, t_n)$ is the Fourier transform of the nonlinear convection term, and \hat{f} is the Fourier transform of the deterministic forcing term.

Recall that in Section 3, we have the ground truth of the correction term $G^\dagger(\mathbf{x}, t) = \nu \nabla^2 \omega(\mathbf{x}, t) + 2\beta\xi$, the above equation can be rewritten as

$$\begin{aligned} \hat{\omega}(k, t_{n+1}) &= \frac{\hat{\omega}(k, t_n) - \Delta t \hat{F}_n + \Delta t \hat{f}(k) + \frac{\Delta t}{2} \hat{G}^\dagger(k, t_n)}{1 + \frac{\Delta t}{2} \nu C} \\ &\approx \frac{\hat{\omega}(k, t_n) - \Delta t \hat{F}_n + \Delta t \hat{f}(k) + \frac{\Delta t}{2} \hat{G}(k, t_n)}{1 + \frac{\Delta t}{2} \nu C}, \end{aligned} \quad (\text{B.7})$$

which represents using our surrogate model G to simulate the 2-D Navier-Stokes system shown in Section 3.3.

Appendix C. Training and Sampling Algorithms

For illustrating the algorithms to train the score-based generative model and to sample from it, we consider the VE SDE shown in Eq. (4) as an concrete example. Its corresponding Gaussian perturbing kernel and reverse SDE are given in Eq. (6) and Eq. (13), and the training and sampling algorithms are presented below.

Algorithm 1: Training

- 1: **repeat**
 - 2: $U_0, y \sim p(U_0, y)$
 - 3: $\tau \sim \mathcal{U}(0, T)$
 - 4: $\epsilon \sim \mathcal{N}(0, I)$
 - 5: $U_\tau = U_0 + \sqrt{\frac{1}{2 \ln \sigma} (\sigma^{2\tau} - 1)} \epsilon$
 - 6: $\mathcal{L}_\tau(\theta) = D_{\text{MSE}} \left(s_\theta(\tau, U_\tau, y), \sqrt{\frac{2}{\sigma^{2\tau} - 1} \ln \sigma} \epsilon \right)$
 - 7: $\theta' = \theta - \nabla_\theta \mathcal{L}_\tau(\theta)$
 - 8: **until** statistical convergence
-

Algorithm 2: Sampling

- 1: $U_T \sim \mathcal{N} \left(0, \frac{1}{2 \ln \sigma} (\sigma^{2T} - 1) I \right)$
 - 2: Set $\tau_{\max} = T, \tau_{\min} = 10^{-3}, \rho = 7$
 - 3: **for** $i = 0$ to $N - 1$ **do**
 - 4: $\tau_i = \left(\tau_{\max}^\rho + \frac{i}{N-1} \left(\tau_{\min}^\rho - \tau_{\max}^\rho \right) \right)^\rho$
 - 5: **end for**
 - 6: Set $\tau_N = 0$
 - 7: **for** $i = 0$ to $N - 1$ **do**
 - 8: $\Delta\tau = \tau_i - \tau_{i+1}$
 - 9: $\epsilon \sim \mathcal{N}(0, I)$
 - 10: $U_{\tau_{i+1}} = U_{\tau_i} + \sigma^{2\tau_i} s_\theta(\tau_i, U_{\tau_i}, y) \Delta\tau + \sigma^{\tau_i} \sqrt{\Delta\tau} \epsilon$
 - 11: **end for**
-